Astronomy & Astrophysics manuscript no. Laurikainen_AA_2016_28936_astro-ph_small
September 8, 2016
©ESO 2016

Barlenses and X-shape features compared: different manifestations of Boxy/Peanut bulges

E. Laurikainen[1] and H. Salo[1]

Astronomy Research Unit, University of Oulu, FI-90014 Finland
e-mail: eija.laurikainen@oulu.fi

Received: 14.5.2016, accepted: 31.8.2016

arXiv:1609.01936v1 [astro-ph.GA] 7 Sep 2016

ABSTRACT

Context. Morphological characteristics of Boxy/Peanut bulges are studied, in particular whether most of the flux associated to bulges in galaxies with masses similar to those of the Milky Way at redshift z~0, could belong to vertically thick inner part of the bar, in a similar manner as in the Milky Way itself. At high galaxy inclinations such structures manifest as Boxy/Peanut/X-shape features, and near to face-on view as barlenses. We also study the possibility that bulges in some fraction of unbarred galaxies could form in a similar manner as the bulges in barred galaxies.

Aims. We use the Spitzer Survey of Stellar Structure in Galaxies (S^4G) and the Near-IR S0 galaxy Survey (NIRS0S), to compile complete samples of galaxies with barlenses (N = 85), and X-shape features (N = 88). A sample of unbarred galaxies (N = 41) is also selected, based on similarity in their surface brightness profiles with those of barlens galaxies. Sizes and minor-to-major axis ratios (b/a) of these presumably vertically thick inner bar components are compared, and interpreted by means of synthetic images using N-body simulation models. Barlenses and their parent galaxies are divided into different sub-groups. Their possible parent galaxy counterparts in galaxies where the barlenses are manifested as X-shape features, are also identified.

Methods. Unsharp mask images are created for all 214 sample galaxies. These images are used to recognize the X-shape features, and to measure their linear sizes, both along and perpendicular to the bar. For detecting possible boxy isophotes (using B_4 -parameter), isophotal analysis is also performed for the barlens galaxies. In the interpretation N-body simulations from Salo & Laurikainen (2016) are used: the models, exhibiting Boxy/Peanut/X/barlens morphologies, are viewed from isotropically chosen directions, covering the full range of galaxy inclinations in the sky. The created synthetic images are analyzed in a similar manner as the observations.

Results. This is the first time that the observed properties of barlenses and X-shape features are directly compared, over a large range of galaxy inclinations. A comparison with the simulation models shows that the differences in their apparent sizes , $a/r_{bar} \gtrsim 0.5$ for barlenses and $a/r_{bar} \lesssim 0.5$ for X-shapes, can be explained by projection effects. Observations at various inclinations are consistent with intrinsic $a_{bl} \approx a_X \approx 0.5\ r_{bar}$: here intrinsic size means the face-on semimajor axis length for bars and barlenses, and the semilength of X-shape when the bar is viewed exactly edge on. While X-shapes are quite common at intermediate galaxy inclinations (for i = 40° - 60° their frequency is ~ half of barlenses), they are seldom observed at smaller inclinations. This is consistent with our simulation models which have a small compact classical bulge producing a steep inner rotation slope, whereas bulgeless shallow rotation curve models predict that X-shapes should be visible even in face-on geometry. The steep rotation curve models are also consistent with the observed trend with B_4 being positive at low inclination, and getting negative values for $i \gtrsim 40°$-60°, thus implying boxy isophotes. In total, only about one quarter of barlenses (with $i \leq 60°$) show boxy isophotes.

Conclusions. Our analysis are consistent with the idea that barlenses and X-shape features are physically the same phenomenon. However, which of the two features is observed in a galaxy depends, not only on galaxy inclination, but also on its central flux concentration. The observed nearly round face-on barlens morphology is expected when at least a few percents of the disk mass is in a central component, within a region much smaller than the size of the barlens itself. Barlenses participate to secular evolution of galaxies, and might even act as a transition phase between barred and unbarred galaxies. We also discuss that the large range of stellar population ages obtained for the photometric bulges in the literature, are consistent with our interpretation.

Key words. Galaxies – photometry – structure – evolution – elliptical and lenticular, cD – individual

1. Introduction

What is the amount of baryonic mass confined into the bulges of galaxies and how was that mass accumulated, is a critical question to answer while constructing models of galaxy formation and evolution. The answer to this question depends on how well the different bulge components can be recognized, and assigned to possible physical processes making those structures. Most of the bulge mass associated to photometric bulges (ie. flux above the disk) is generally assumed to reside in classical bulges. These are relaxed, velocity dispersion supported structures, presumably formed by galaxy mergers (White & Rees 1978; Hopkins et al. 2009), or by coalescence of massive star forming clumps at high redshifts, drifted towards the central regions of the galaxies (Bournaud et al. 2008; Elmegreen et al. 2009; see also review by Kormendy 2016). This picture has been challenged by the discovery that most of the bulge mass in the Milky Way actually resides in a Boxy/Peanut (B/P) bar, showing also evidence of an X-shape morphology, without any clear evidence of a classical bulge (McWilliam & Zoccali 2010; Nataf et al. 2010; Wegg & Gerhard 2013; Ness & Lang 2016). Whether such bar-related inner structures could form most of the bulge mass also in external Milky Way mass galaxies is a topic of this study.

Boxy/Peanut (B/P) bulges are easy to distinguish in the edge-on view and it has been shown that even 2/3 of all disk galaxies

in S0-Sd types have B/Ps (Lütticke, Dettmar & Pohlen 2000; Bureau et al. 2006; but see also Yoshino & Yamauchi 2014). Many B/P bulges also show cylindrical rotation (Kormendy & Illingworth 1982; Bureau & Freeman 1999; Falcón-Barroso et al. 2006; Molaeinezhad et al. 2016; Iannuzzi & Athanassoula 2015), which generally confirms their bar origin. Verification of a galaxy as barred is difficult in the edge-on view, but it has been shown that, at an optimal range of viewing angles, B/Ps are visible even in less inclined galaxies, as revealed by their boxy isophotes (Beaton et al. 2007; Erwin & Debattista 2013, hereafter ED2013). A new morphological feature, a barlens (bl), was recognized by Laurikainen et al. (2011), and it has been suggested (Laurikainen et al. 2014, hereafter L+2014; Athanassoula et al. 2015, hereafter A+2015; see also Laurikainen et al. 2007) that they might be the face-on counterparts of B/P bulges. Association of a barlens to the Milky Way bulge has been recently made by Bland-Hawthorn & Gerhard (2016).

Because of their fairly round appearance barlenses are often erroneously associated with classical bulges (see the review by Laurikainen & Salo 2016), but there is cumulative evidence showing that barlenses might indeed form part of the bar. Their optical colors are very similar to the colors of bars (Herrera-Endoqui et al. 2016, hereafter HE+2016), and in particular, their surface brightness profiles are very similar to those predicted for the B/P-bulges in hydrodynamical simulation models when viewed face-on (A+2015). The first indirect observational evidence connecting barlenses with B/P bulges (which often have X-shape features in unsharp mask images), was based on the axial ratio distribution of the combined sample of their parent galaxies, which appeared to be flat (L+2014). However, it remained unclear why barlenses concentrate on earlier Hubble types than the B/P/X-shape bulges (peak values are T = -1 and T = +1, respectively). Is this simply an observational bias when classifying galaxies at low and high inclinations, or could it indicate some intrinsic difference between the parent galaxies hosting barlenses and X-shape features? The latter possibility is suggested by the recent N-body simulations by Salo & Laurikainen (2016; submitted to ApJ), who demonstrated that a steep inner rotation curve leads to realistic-looking round barlens morphology, with no trace of an X-shape in the face-on geometry. However, reducing the central mass concentration, and thus shifting the galaxy to a later Hubble type, produced more elongated barlenses, which exhibited X-features at a much larger range of galaxy inclinations.

As barred and unbarred galaxies presumably appear in similar galaxy environments (see Aquerri, Méndez-Abreu & Corsini 2009), it is not plausible that bulges in barred galaxies form smoothly by secular evolution, and bulges in unbarred galaxies by some violent processes, like major galaxy mergers. Therefore, our hypothesis that many classical bulges are misclassified B/P/X features can be valid only if an explanation is found also for the bulges of unbarred galaxies, in the same line with the explanation for the barred galaxies. In fact, there is observational evidence which hints to that direction. Namely, the inner lenses (normalized to galaxy size) in unbarred galaxies are shown to have similar sizes as barlenses in barred galaxies (Laurikainen et al. 2013; Herrera-Endoqui et al. 2015, hereafter HE+2015). Inner lenses in unbarred galaxies might therefore represent evolved bars where the thin bar component has been completely dissolved, or the classical elongated bar never formed. However, whether those lenses are also vertically thick needs to be shown.

In this study the properties of 85 barlenses and their parent galaxies are studied, and compared with the properties of 88 galaxies hosting bars with X-shape inner feature. An additional sample of 41 unbarred galaxies is also selected. As a database we use the Spitzer Survey of Stellar Structure in Galaxies (Sheth et al. 2010), and the Near-IR S0 galaxy Survey (Laurikainen et al. 2011). The properties of the analyzed features are compared with those obtained for synthetic images, created from simulation models taken from Salo & Laurikainen (2016). To obtain a fair comparison, the analysis for the synthetic images is done in a similar manner as for the observations.

2. Data and the sample selection

The Spitzer Survey of Stellar Structure in Galaxies (S^4G, Sheth et al. 2010) is a sample of 2352 nearby galaxies observed at mid-IR wavelengths, covering all Hubble types and disk inclinations. The galaxies have HI radial velocities $V_{radio} < 3000$ kms^{-1} corresponding to the distance of D < 40 Mpc for $H_\circ = 75$ km s^{-1}, and blue photographic magnitudes $B_T \leq 15.5$ mag. The Near-IR S0 galaxy Survey (NIRS0S, Laurikainen et al. 2011) is a survey of 185 S0-Sa galaxies, having magnitudes $B_T \leq 12.5$, and galaxy inclinations of $i \leq 65°$ (N = 215 if included are also the galaxies which slightly exceed the magnitude-limit). The morphological classifications of the S^4G galaxies are from Buta et al. (2015), and those of NIRS0S from Laurikainen et al. (2011) using the same classification criteria. The wavelengths used in the above classifications are 3.6 μm in S^4G, and 2.2 μm in NIRS0S: both are fairly dust free regimes allowing to recognize the morphological features of the old stellar population.

The quality of the images is explained by Laurikainen et al. (2011) for NIRS0S, and by Salo et al. (2015), Querejeta et al. (2015), and Muńoz-Mateos et al. (2015) for the S^4G images. The NIRS0S images typically have pixel resolution of 0.25 arcsec, FWHM ~ 1 arcsec, and FOV of 4-5 arcmin. The images typically reach a surface brightnesses of 23 mag arcsec^{-2} in K_s, equivalent to 27 mag arcsec^{-2} in the B-band. The S^4G images have a pixel resolution of 0.75 arcsec, and FWHM 2.1 arcsec, and they reach a surface brightness of 27 AB (1σ) mag arcsec^{-2} at 3.6 μm (equivalent to roughly 28 mag arcsec^{-2} at the B band). For large galaxies the S^4G images are mosaics, covering at least 1.5 x D_{25}, where D_{25} is the isophotal size of the galaxy in B-band.

From the combined S^4G + NIRS0S sample all barred galaxies with a barlens (bl) in the classification were selected, which makes 84 barlens galaxies. We added to this category also NGC 1433 which clearly has a barlens, although it is missing in the original classification. For the recognition of the X-shape features unsharp masks were first done for all the S^4G and NIRS0S galaxies: weak X-features can be recognized from unsharp mask images even if they were not visible in the direct images. This makes 88 galaxies with identified X-shape features. In 6 of the galaxies both a barlens and an X-shape feature were identified. We also selected a sample of 41 largely unbarred galaxies which have similar exponential surface brightness profiles as barlenses typically have. Those galaxies can have inner lenses or ringlenses (34 galaxies), but not all of them have. A few of them are classified as weakly barred (AB) by Buta et al. (2015). The final samples are:

(1) galaxies with barlenses (N = 85)
(2) galaxies with X-shape features (N = 88)
(3) unbarred galaxies (N = 41)

Compared to the total number of galaxies in our starting S^4G+NIRS0S sample the numbers for the barlens and X-shape galaxies are fairly small. This is mainly because S^4G, being a

magnitude limited sample, is dominated by low luminosity late-type galaxies, whereas the B/P/bl features typically appear in bright galaxies with strong bars: of the bright galaxies ~ 2/3 have bars and only a half of the bars are strong. It was shown by L+2014 that while concentrating on galaxies with -3 ≤ T ≤ -2, i <65°, and B_T < 12.5 mag, ~ 46% of the barred galaxies in our sample have either a barlens or an X-shape feature.

The inclination distribution of the galaxies in our combined sample has been previously studied by L+2014. Although barlenses are preferentially concentrated to galaxies with low inclinations, and the X-shapes to galaxies with high inclinations, there is a large overlap in their parent galaxy inclinations. This makes our sample ideal for comparing the properties of these structures. The three selected samples are shown in Tables 1, 2 and 3. In the tables given are also the morphological classifications from Buta et al. (2015). If the galaxy does not appear in S^4G the classification is from Laurikainen et al. (2011). For the following galaxies differences appear in the above classifications: for NGC 584 SA(l)0$^-$(NIRS0S) / E(d)(S^4G), for NGC 5631 SA(l)0$^-$(NIRS0S) / E0-1(S^4G), and for NGC 5646 SA(l)0$^-$(NIRS0S) / E0-1(S^4G). For these galaxies both classifications are given.

The sizes of bars and barlenses are from HE+2015 and HE+2016, respectively. The orientation parameters and the scale lengths of the disks are from Salo et al. (2015). For bars visual length estimates are used, because they are measured in a homogeneous manner for all galaxies in our sample. In HE+2015 and in Díaz-García et al. (2016a) it was shown that the visual bar length estimates are fairly similar to those obtained from the maximum ellipticity in the bar region.

3. Methods

3.1. Unsharp masks

In this study unsharp mask images for the complete sample of 214 galaxies were done. For the galaxies with X-shaped bars we end up to the same sample as used by L+2014. The images were first convolved with a Gaussian kernel (mean σ ~ 4 arcsec), and the original images were then divided with the convolved images. In order to show possible low surface brightness structures special attention was paid to find optimal parameters to illustrate the morphologies. Widths of the Gaussian kernels that best illustrated the faint features were found empirically by inspecting a large range of values for each galaxy. Our Gaussian convolution method avoids possible artifacts that might appear in the simple approach where the images are divided by rebinned images. The original and unsharp mask images, as well as the surface brightness profiles for the sample of 214 galaxies are shown in electronic form (/www.oulu.fi/astronomy/BLX/) The electronic file is organized in the following manner, with an increasing NGC number in each group:

1. Strongly barred with a barlens (bl_B)
2. Weakly barred
 a) barlens in the classification (bl_{AB})
 b) no barlens in the classification, but has a barlens-like surface brightness profile (AB)
3. Unbarred
 a) have an inner lens (A_l)
 b) no inner lens appears, but similar surface brightness profile as in a barlens (A_{expo})
4. Have bl in classification and X in the unsharp mask (bl-X)
5. X-shaped bar (X)

The first three primary groups are selected based on the bar family (B, AB, A), whereas the last two groups appear to be mixtures of strongly and weakly barred galaxies, having similar numbers of both families. NGC 3384 is shown using both in K_s and 3.6 μm images, in which bands the galaxy shows very different morphology in the central regions: in K_s a central peak appears, whereas at 3.6 μm the galaxy has a bright dispersed central region and a drop of flux in the very center. The same web-page contains also files illustrtaing various barlens sub-groups (defined in Section 6.1), and the sub-groups for their parent galaxies (defined in Section 6.2). For the galaxies both sky and deprojected images are shown.

3.2. Size measurements of the X-shape features

Using the obtained unsharp mask images (in the sky plane) the sizes of the X-shape features were measured and collected to Table 2, where the orientation in respect of the "thin bar" is also given. An example illustration is shown in Figure 1: the four corners of the X are marked on the image, and the semi-lengths of the feature along the bar (a), and perpendicular to it (b) are obtained as mean values of the extents of the two sides. In order to facilitate the measurements the images were first rotated so that the bar appeared horizontally. Generally the X-shape features are clear (see NGC 2654), but particularly in the end-on view the 'horns' making the X are very weak. The measurements were repeated three times, and the mean values together with their errors (standard deviation of measurements divided by $\sqrt{3}$; typically less than 0.5 arcseconds) are indicated. Sizes of barlenses are taken from the previous measurements (HE+2016; their Table 2), where they were obtained by fitting ellipses to the points delineating the outer isophotes of the barlenses: this gives the semilengths along the major (a) and minor axis (b) of the barlens, and the orientation of the major axis. The uncertainties were estimated in a similar manner as our uncertainties for the X-shape dimensions.

3.3. Making synthetic images and showing them at different viewing angles

For making the synthetic images we use N-body simulation models from Salo & Laurikainen (2016). These simulations, performed with Gadget-2 (Springel & Hernquist 2005), addressed the influence of central mass concentration on the formation of barlens features. In comparison to the N-body + SPH simulation models by Athanassoula et al. (2013, 2015), the models are much simpler, consisting of only the stellar components: a small pre-existing classical bulge, an exponential disk, and a spherical halo. No gas or star formation were included. At two scalelengths (h_r), the disk accounts for 65% of the total radial force, the initial vertical thickness of the disc is $0.2 \cdot h_r$, and the Toomre parameter Q ~ 1.3. We select snapshots from two simulations, both about 3 Gyrs after the bar has been formed and stabilized in strength. The two models differ in their bulge-to-disk (B/D) mass ratios at the beginning of the simulation, so that the model with B/D = 0.01 is practically bulgeless, whereas the other model has a small bulge with B/D = 0.08. The effective radius of the bulge was fixed to $r_{eff}/h_r = 0.07$, which is the typical observed value to T = 3 galaxies (Salo et al. 2015). Both models develop a B/P/X bulge, and in particular in the model with larger B/D the resemblance to the typical face-on barlens morphology is very good. The only difference here to the simulations displayed in Salo

& Laurikainen (2016) is that we have increased the number of particles by a factor of 5, in order to improve the quality of the synthetic images: the behavior of the models is practically unaffected by the increased particle number.

In order to have a representative sample of galaxy orientations in the sky-plane, the two simulation snapshots were viewed from 100 isotropically chosen directions. In practice this was done by viewing the galaxy first from its pole ($i = 0°$), and then spiraling around the galaxy with suitably selected constant steps in azimuthal angle ϕ and cos i (we used $\Delta\phi = 41.4°$, and $|\Delta \cos i| = 0.02$). The angle ϕ is counted from the direction of the bar major axis. These images for the model with B/D = 0.08 are shown in Figure 2. Barlenses and X-shape features in the synthetic images were measured in a similar manner as in the observations.

In Figures 3-5 we show how the morphology of the vertically thick inner bar component varies with the viewing angle. In all these figures the left panels show the images, in the middle panels the isophotal contours are overlaid, and the right panels show the unsharp masks of the same images. The line-of-node is always horizontal. The simulation had $5 \cdot 10^6$ disk particles, and to increase the S/N of the synthetic images, three simulation snapshots were superposed, after rotating the bar to the same orientation. Moreover, we made use of the reflection symmetry with respect to the equatorial plane, and the m = 2 rotational symmetry with respect to 180° rotation in the equatorial plane. The effective number of disk particles in the synthetic image thus corresponds to $60 \cdot 10^6$. In Figure 3 the simulation models for B/D = 0.01 and 0.08 are shown at five different inclinations keeping the azimuthal viewing angle fixed to $\phi = 90°$. In Figure 4 the inclination is fixed to $i = 90°$: in the different panels the azimuthal angle varies from the end-on ($\phi = 0°$) to side-on view ($\phi = 90°$). Also in Figure 5 the azimuthal angle varies, but the inclination is fixed to $i = 60°$.

The sizes of the X-shape and barlens features measured from the simulated images are compared with the observations in Section 5. Here we emphasize some morphological differences depending on the viewing angle. Figure 3 shows that in the simulation model with B/D = 0.01 the X-shape is at some level visible at all galaxy inclinations in the unsharp mask images, showing also peanut-shaped isophotes in the direct images. In the model with B/D = 0.01 the size of the X-feature also decreases towards lower galaxy inclinations. However, when B/D = 0.08 the X-shape disappears when the inclination gets smaller than $i = 30°$-45° (also, the isophotes are not boxy anymore).

When fixing the inclination to $i = 90°$ and allowing the azimuthal angle to vary (Fig. 4) some morphological differences also appear: as expected the size of the X-feature shrinks towards the end-on view ($\phi = 0°$). The X-feature is always present in the B/D = 0.01 model, whereas in the model with B/D = 0.08 it disappears in the end-on view. Another comparison with varying azimuthal angle, but this time fixing the inclination to $i = 60°$, is also interesting: in the bulgeless model the X-shape gradually decreases in size, and finally disappears near the end-on view (Fig. 5). On the other hand, in the B/D = 0.08 model the X-shape feature rapidly disappears with a decreasing azimuthal angle and it starts to resemble a barlens: depending on the azimuthal angle it looks like a spheroidal ($\phi = 0°$), or the "thin bar" appears as two twisted spiral-like features outside the barlens ($\phi = 30°$- 40°). Also ansae can be identified is some of those bars at $\phi = 30°$- 40°.

3.4. Isophotal analysis of barlenses

We made isophotal analysis for the sample galaxies using the IRAF ellipse routine. It provides the parameters A_4 and B_4 which are associated to the sin 4θ and cos 4θ terms of the Fourier expansion of the isophotal shape, respectively. The fourth order coefficients (A_4 and B_4) are generally used as descriptors of the deviations of the isophotes from simple ellipses: they are boxy when $B_4 < 0$ and $A_4 > 0$, and disky when $B_4 > 0$ and $A_4 < 0$. The best evidence of boxiness can be obtained using the B_4 parameter. In the boxy bar region PA is maintained nearly constant, and ϵ gradually increases towards the outer edge of the bar (see Beaton et al. 2007). In this study the radial profiles of B_4, together with the profiles of the position angle (PA) and ellipticity (ϵ = 1-b/a) in the bar regions were derived for all barlens galaxies, of which an example is shown in Figure 6. In the surface brightness profile the boxy bar forms part of the photometric bulge. If the barlens is boxy it is marked in Table 1, based on visual inspection of the isophotes and the B_4 profile. The table indicates also the mean and standard deviation of B_4 in the barlens region. The importance of higher order Fourier modes for identifying X-shape features, particularly at high galaxy inclinations, has been discussed by Ciambur (2015). However, barlens galaxies in our sample do not have such high galaxy inclinations (the highest galaxy inclination is 72°). We find by visual inspection that only roughly one-quarter (19/79) of the barlenses have boxy isophotes.

In Figure 7 the obtained $< B_4 >$ values are shown: the red and green colors indicate our visual detection/non-detection of the boxy isophotes, respectively, being in good agreement with the mean $< B_4 >$. Also shown are the B_4 values for the synthetic images using the simulation model with B/D = 0.08. It appears that both in observations and in synthetic images the detection fraction of boxy isophotes increases with galaxy inclination, so that the isophotes start to appear boxy at $i \gtrsim 45°$. We have chosen the model with B/D = 0.08, because for this model the vertically thick bar component manifests as a barlens for a large range of galaxy inclinations. This B/D value is also close to that obtained for the 'true' bulge components of barlens and X-shaped galaxies in the multi-component decompositions by L+2014, carried out for a small but representative sample of 29 barlens/X-shaped galaxies. For the $B/D = 0.01$ model the mean B_4 in the inner bar region would be negative for all galaxy inclinations, consistent with its X-shape morphology (see Figs. 3–5, and Fig. 21 below).

Similar figures as Figure 6 are given for the all barlens galaxies in electronic form at /www/astronomy/BLX..

4. Comparison of barlenses and X-shape features

The sizes of barlenses and X-shape features are compared in Figure 8. The parameters are shown in the sky plane because it is not possible to deproject the highly inclined X-shaped galaxies in a reliable manner. It appears that the sizes of both features correlate with r_{bar} (upper panel) so that the size increases with r_{bar}. However, the X-shape features are clearly smaller than barlenses (the uncertainty of both bl and X measurements is comparable to the size of the plotting symbols). The scatter is also larger for the X-shape features, which is not unexpected having in mind that they appear at larger galaxy inclinations, and because the apparent size depends also on the angle between the X-shape and the bar major axis in a specific viewing angle. For both features the normalized (normalization to r_{bar}) sizes are constant as a function of the parent galaxy mass (lower panel), which means that the size difference is not a mass effect. The galaxy masses are

from Muńoz-Mateos et al. (2015), derived from the 3.6 μm and 4.5 μm images, based on mass-to-luminosity ratios from Eskew, Zaritsky & Meidt (2012).

Our size measurements for the X-shape features (a/r_{bar} ~0.2–0.5, $<a/r_{bar}>$~0.35) agree well with a/r_{bar} ~ 0.4 given for the B/P structures, in the edge-on view by Lütticke, Dettmar & Pohlen (2000), and at intermediate galaxy inclinations by ED2013. It will be discussed in Section 9.1, that the boxy bulges by ED2013 are actually the same entities as what we call X-shapes, for which reason such an agreement is expected.

Histograms of the minor-to-major axis ratios of barlenses and X-shape features are compared in Figure 9. In our combined S^4G + NIRS0S sample barlenses have b/a = 0.4–1.0 (upper panel), which is in agreement with that shown previously for the NIRS0S galaxies by A+2015. The peak value in the sky-plane is ~ 0.75, which in the disk plane is shifted to ~0.85. A majority of the X-shape features appear in the same b/a-range with barlenses (lower panel). However, there is no reason why the ratios should be exactly the same. For example, in the X-shape features there is a wing towards larger b/a. The galaxies in this wing are IC 1711, IC 3806, NGC 4419, NGC 4565, NGC 5145, NGC 5746, NGC 5757 and NGC 5777. Five of these galaxies have high parent galaxy inclinations (i = 70°- 80°), in which galaxies the bar most probably is seen nearly end-on. A well known example of nearly end-on galaxies is NGC 4565, discussed also by Kormendy & Barentine (2010). In fact, the morphology of the X-shape in NGC 4565 is very similar to our B/D = 0.08 synthetic image in Figure 4, seen close to the end-on view (ϕ = 30°, i = 90°). The three remaining galaxies have lower inclinations (i = 33°, 40° and 65°, respectively). One of them, NGC 5145, has no detection of a bar, and in the two barred galaxies, IC 3806 and NGC 5757, the X-shape features are among the weakest detected in our sample.

5. Comparison of observations and synthetic images

We compare the observations and synthetic images in order to study to which extent galaxy inclination affects the major-to-minor axis ratios, and the normalized sizes of barlenses and X-shape features. The comparison is shown in Figure 10 where the observations are shown on the left, and the synthetic images on the right.

The axis ratios of barlenses and X-shape features (in the sky plane) are shown as a function of galaxy inclination in the lower panels of Figure 10. A qualitative agreement between the observations and synthetic images is good: b/a gradually decreases towards higher galaxy inclinations until the images are seen nearly edge-on, where b/a increases again. Also, barlenses and X-shape features, both in the observations and in the synthetic images, form a continuation as a function of galaxy inclination. This behavior is independent of the simulation model used.

More informative is to look at the normalized sizes of the structures (upper panels). It appears that the size of a barlens is on average constant at i = 0° – 50°, increasing towards higher galaxy inclinations (i = 50° – 65°). Also, the X-shapes have a constant size at low galaxy inclinations, whereas at high inclinations both small and large sizes appear. Qualitatively similar tendencies can be found also for the synthetic images. However, it is important to consider the two models separately: although in both models barlenses have similar sizes, differences appear in the sizes of their X-shape features. In the bulge model (B/D = 0.08) the X-shapes are manifested only at i > 50°, where the sizes are also more similar to those of barlenses. The arrows indicate where barlenses in the face-on view, and X-shape features in the edge-on view in this model, have similar sizes. On the other hand, in the bulgeless model (B/D = 0.01) small X-shapes appear even in almost face-on view (i = 20° – 40°). The size gradually increases towards higher galaxy inclinations. Inspecting the morphology of the vertically thick inner bar components in the synthetic images helps to better understand the above differences between the two models: the bulge model (B/D = 0.08) is lacking small X-shapes in the face-on view because at those inclinations the morphology is turned into a barlens morphology (see Fig. 3). Also, even at higher galaxy inclinations (i = 60° inspected in Fig. 5) small X-shapes are not visible if the azimuthal angle of the bar is large.

6. Morphology of barlens galaxies

6.1. Division of barlenses to sub-groups

Barlenses do not form a homogeneous group of features, most probably reflecting the fact that they consist of a combination of orbital families of bars, with a range of different orbital energies. In order to further investigate their morphologies barlenses are divided to sub-groups. Our intention is not to classify all barlens galaxies, but rather to pick up prototypical cases with clear morphological characteristics. Examples of those groups are shown in Figures 11 and 12: the left panels show the original 3.6 μm or K_s-band images, cut in such a manner that they best show the bar region. With the same image cuts also shown are the unsharp mask images, in the sky-plane and when deprojected to the disk plane. The surface brightness profiles as a function of the isophotal semimajor axis are also shown, together with the profiles along the bar major and minor axis. However, if i > 65° only the bar major axis profiles are shown. The following subgroups were recognized:

Group a: *a regular "thin bar" is a characteristic feature; on top of that a round barlens appears.* Outside the central peak the barlens has an exponential surface brightness profile, both along the bar major and minor axis. The "thin bar" is prominent and penetrates deep into the central regions of the galaxy. The surface brightness profile along the bar major axis continues without cutoffs until the end of the bar. Good examples of this group are: NGC 1015, NGC 1452, NGC 4608 and NGC 4643. As an example shown is NGC 4643 in Figure 11, discussed previously also by L+2014.

Group b: *a large barlens dominates the bar; it has a small-scale structure at low surface brightness levels, which structure is typically elongated along the bar major-axis*. Prototypical cases are NGC 5101 shown in Figure 11, and NGC 4314 discussed by L+2014 (see their Fig. 1). Other galaxies belonging to this group are: NGC 1512, NGC 4245, NGC 4394, NGC 4596, NGC 5375, and with some reservation also NGC 1640. In many galaxies in this group the "thin bar" is manifested only as tips at the two ends of the bar. In NGC 4314 the "thin bar" is clumpy at low surface brightness levels.

Group c: *barlens has two components, a bright "inner disk" and a low surface brightness structure outside that feature.* The "inner disk" is still larger than typical nuclear bars or rings, and it is generally oriented along the underlying large-scale disk. Examples are NGC 1398, NGC 2787, NGC 3945, NGC 4262, NGC 4371, NGC 4754 and NGC 3384, and possibly also NGC 3489. As an example shown is NGC 1398 (Fig. 11). This is a

group of barlens galaxies with the lowest fraction of inner rings or ringlenses (only 33% have r/rl).

Group d: *barlens and the "thin bar" have low surface brightnesses compared to that of the underlying disk*. The central regions of all these galaxies are dominated by strong nuclear bars, nuclear rings or lenses, or by a few star forming clumps as in NGC 7552. The strong star forming regions are well visible at 3.6 μm wavelength. Good examples are NGC 613, NGC 1097, NGC 1300, NGC 5728, and NGC 7552, of which NGC 1300 is shown in Figure 11.

Group e: *barlens dominates the bar; it is round and covers most of the bar size. The "thin bar" often ends up to ansae (appear in classification by Buta et al. 2015) at the two ends of the bar*. Examples of strong bars (B) are: NGC 936, NGC 1440, NGC 1533, NGC 2983, NGC 3941, NGC 3992, NGC 4548, NGC 4340, NGC4579, NGC 5770 and NGC 6654. Examples of weak bars (AB) are: NGC1291, NGC 1326, NGC 2859, and NGC 6782. All these weak bars have also nuclear bars, often surrounded by nuclear rings. With uncertainty, included to this group are also the galaxies: NGC 3892, NGC 3953 and NGC 4143. Our example of strong bars is NGC 4548, and of weak bars NGC 1291 (Fig. 12).

Group f: *barlens dominates the bar which ends up to two tightly wound spiral arms*. Good examples are NGC 1079, NGC 1350, NGC 2273, NGC 2543, NGC 3368 and NGC 5026. In Figure 12 NGC 2273 is shown.

Group g: *barlens dominates the bar to such a level that barely no "thin bar" appears.* All these galaxies are weakly barred (AB), and except for NGC 5750, have no inner rings. Examples are: NGC 1302, NGC 2293, NGC 4503, NGC 4659, NGC 4984, NGC 5750, and NGC 6684, and with some reservation also NGC 1022. NGC 4503 has no barlens in the classification by Buta et al. (2015), but the galaxy has similar morphology as the other galaxies in this group. NGC 4659 has also an X-shape feature in the unsharp mask image. The surface brightness profiles of these galaxies resemble those of unbarred early-type galaxies (see Laurikainen et al. 2009, 2010). As an example NGC 2293 is shown (Fig. 12).

Galaxies in the groups a – d are largely strongly barred (B), in the group e both strong and weak bars appear, whereas galaxies in the groups f-g are weakly barred (AB). The classified galaxies in the different barlens groups are shown at /www/astronomy/BLX.

6.2. Division of barlens parent galaxies to sub-groups

As barlenses, also their parent galaxies can be divided to subgroups, based on their characteristic morphological features. The following groups were recognized (see Fig. 13), ordered according to an increasing dominance of later Hubble types:

Group 1: *S0-S0/a, mainly S0°;* the "thin bar" is very weak (1a), or it is dominated by ansae at the two ends of the bar (1b). Most of these galaxies have outer lenses (L) or ringlenses (RL) (in 88%; in 100% if uncertain galaxies are excluded). Example galaxies having a shallow thin bar are: NGC 1440, NGC 1533, NGC 3266, NGC 3489, NGC 4659, NGC 5750, NGC 5838, NGC 6684. Bars with ansae are: NGC 2787, NGC 2983, NGC 3941, NGC 4143, NGC 4262, NGC 4754, NGC 7079. Uncertain cases are NGC 1201 and NGC 2293, which galaxies have no L or RL. In Figure 13 shown are NGC 1440 (1a) and NGC 2787 (1b).

Group 2: *S0$^+$-S0/a, mainly S0$^+$*; an inner lens (or ringlens) fills the space inside the bar radius. The galaxies in this group almost always have also outer rings (R) or outer lenses (L). Good examples are: NGC 1079, NGC 1291, NGC 1302, NGC 1326, NGC 2859, NGC 2968, NGC 3380, NGC 3637, NGC 3945, NGC 4984, NGC 5134, NGC 5701, NGC 5728, and NGC 6782. In the galaxies NGC 1512 and NGC 1350 the region inside the bar radius is somewhat less crowded. As an example NGC 2859 is shown.

Group 3: *S0-S0/a, mainly S0/a*; these are strongly barred galaxies in which the bar ends up to sharp features, which can be arcs or rs-type inner rings. As in group 2, also all these galaxies have outer rings (R) or lenses (L). Good examples are: NGC 936, NGC 1015, NGC 4596, NGC 4643, NGC 5101, and NGC 5375, of which NGC 4643 is shown.

Group 4: *S0-Sab, mainly Sa*; a strong bar ends up to a prominent, fully developed inner ring (r), which is the dominant feature of the galaxy. In some of the galaxies ansae also appear in the bar, but due to a superposition with the prominent inner rings they are not always clear. Galaxies in this group have a large range of Hubble types. Good examples are: NGC 1452, NGC 4245, NGC 4340, NGC 4371, NGC 4454, NGC 4608, and NGC 5770, of which NGC 1452 is shown.

Group 5: *S0-Sb, mainly Sa, Sab;* galaxies in this group have two extremely open spiral arms, and a lens-like structure (not an inner lens in galaxy classification) at the bar radius. In some cases the inner feature is a lens (NGC 4314, shown in Fig. 13), and in some cases spiral arm segments around the bar (NGC 613 and NGC 1097). The lens in NGC 4314 is not as inner lenses in galaxy classification, being more elongated along the bar major axis. Other examples of this group are NGC 3368, NGC 4593 and NGC 7552.

Group 6: *Sa-Sb*; the dominant features are two prominent, tightly wound spiral arms, starting from the two ends of the bar. In distinction to the previous group the inner lens-lihe structure is missing, and the spiral arms are more tightly wound. Good examples are NGC 1300, NGC 2273, NGC 2543, NGC 4795 and NGC 5026. As an example NGC 2273 is shown.

Group 7: *Sab-Sb*; these galaxies have fully or partly developed inner ring (r) surrounding the bar, and the outer disk is dominated by multiple spiral arms. Good examples are NGC 1433, NGC 3351, NGC 3953, NGC 3992, NGC 4639:, NGC 4394, NGC 4902, NGC 5339, NGC 5850, NGC 5957, NGC 7421, IC 1067, and IC 2051. As an example NGC 4902 is shown: the barlens in this galaxy shows also a weak X-shape feature in the unsharp mask image.

The above galaxies identified in the different barlens parent galaxy groups are shown at //www/astronomy/BLX.

6.3. Cross-correlating barlens groups with their parent galaxies

Statistics of the morphological features in the galaxies with different barlens groups are collected to Table 4, and those in the parent galaxy groups to Table 5. A general tendency is that barlens galaxies very often have inner rings or ringlenses. For the barlens sample as a whole the fraction is 78%, and for none of the sub-groups the fractions are below 50%. This fraction is higher in strongly barred and early-type galaxies, being even 100% in the barlens groups a and b. In these particular groups the fraction of ansae is smaller than in the other groups (in groups a and b 12-17% have ansae, in comparison to 33-57% in the other groups).

On the other hand, the fraction of nuclear features is typically high (25-42% have nuclear bars or rings). There is a peak in the fraction of nuclear features in the barlens group d where all galaxies have nuclear bars or rings.

Looking at the parent galaxy groups there is a tendency of increasing galaxy mass from the group 1a towards the group 4, the mean mass increasing from $\log(M^*/M_\odot) = 10.30\pm0.19$ to $\log(M^*/M_\odot) = 10.83\pm0.13$. A minimum in the parent galaxy mass appears in group 4, where $<\log(M^*/M_\odot)> = 10.22\pm0.10$. The uncertainties are stdev/$\sqrt{N}$. Also the groups 2 and 6 have something in common: the bars in these galaxies are typically weak (only 33% belong to B family, compared to 67-100% of strong bars in the other groups). This is in spite of the fact that the galaxies are fairly massive, ie. $<\log(M^*/M_\odot)> = 10.58\pm0.07$ and 10.70 ± 0.10 for the groups 2 and 6, respectively. Common to these two groups is also that the region inside the bar radius is crowded (even more in group 2), and the bars are often surrounded by inner (78%, 50%) and outer (89%, 50%) rings or ringlenses. Inner rings and ringlenses are even more common in the groups 3–5 and 7, where actually all galaxies have such features: in the galaxies of these groups the "thin bars" are prominent which might explain the large number of rings. Bars in the groups 3–5 and 7 do not have frequently ansae (0-33% have ansae, in comparison to 17-100% in other groups). Nuclear features have a peak in the parent galaxy group 5 (86% have nuclear features) .

Barlens and parent galaxy groups are cross-checked in Table 6. The numbers of galaxies in which both groups were identified is fairly small, and there is also a large scatter, but some tendencies can be seen:

Group 5 – Group d: There is a connection between the barlens group d and the parent galaxy group 5: in both groups the bar has a low surface brightness, and the parent galaxy shows two open spiral arms and a lens-like structure at the bar radius. Most probably, due to a fairly shallow potential well these galaxies are efficient in transferring material towards the central regions of the galaxies, triggering nuclear bars, rings or lenses, which are typical in these galaxies. The bars never have ansae. These galaxies have the largest masses among the groups studied by us, ie. $<\log(M^*/M_\odot)> = 10.86\pm0.15$ and $<\log(M^*/M_\odot)> = 10.71\pm0.14$ for the groups d and 5, respectively.

Group 1b – Groups c, e: There is also a connection between barlenses that have bright "inner disks" (barlens group c), and the parent galaxy morphology. Namely, in 3/6 of the groups c/e the "thin bar" is manifested mainly as ansae at the edges of the bar potential (parent galaxy group 1b). The dominant outer features are lenses (L), which appear even in 86% of these galaxies (in comparison to 5-25% in the other parent galaxy groups). On the other hand, inner rings (only 14% have r or rl) and nuclear features (only 14% have nuclear features) are less common than in any of the other parent galaxy groups.

Groups 3,4,7 – Groups a, b: The parent galaxy groups 3, 4, and 7 are associated to barlens groups a and b (4/6, 4/7 and 4/5 of the parent galaxy groups, respectively). These are largely strongly barred galaxies, where the bar is a combination of a prominent classical bar and a prominent barlens. All these galaxies have partly or fully developed inner rings or ringlenses (100%), whereas outer rings appear only in 33-50% of the galaxies.

7. Morphology of the galaxies with X-shaped bars

An interesting question is do the parent galaxies of the X-shaped bars have similar morphologies as the galaxies with barlenses? Because the X-shapes appear in galaxies with higher galaxy inclinations, the observations are more susceptible to dust and therefore any statistics of their structure components is less reliable. However, a general trend is that, in a similar manner as barlenses, also the galaxies with X-shapes typically have inner rings and small inner disks (see also Bureau et al. 2006 for X-shapes in the edge-on view). Such an inner disk is particularly prominent in an X-shaped galaxy NGC 4216, with i=79°, shown in Figure 14.

In Figure 15 we show three galaxies having bars that manifest X-shape features: below each of these galaxies their barlens galaxy counterparts are shown. The first galaxy pair is NGC 7179 (X) / NGC 5101 (bl): both are strongly barred, have a Hubble stage S0/a, and either rl or rs surrounds the "thin bar". In the unsharp mask images the "thin bars" appear mainly as tips in flux at the two ends of the bar potential. Another example pair is IC 1067 (X) / NGC 4643 (bl): in these galaxies the inner rings are complete, and the "thin bars" appear as classical elongated features penetrating deep into the central regions of the galaxies. The third pair is NGC 3673 (X) / NGC 2273 (bl): both are early-type spirals, dominated by a barlens or an X-shape feature, which end up to two tightly wound spiral arms. While looking at the surface brightness profiles of the first two pairs, it is obvious that barlenses have central peaks, which are missing in their X-shaped counterparts. The galaxy with an X-shaped bar in NGC 3673 has stronger central flux concentration than the other X-shaped bars discussed above, but it is still less prominent than in its barlens galaxy counterpart.

In the simulation models discussed in the literature, the X-shape features are generally associated to strong bars in massive galaxies (Athanassoula 2005; Martinez-Valpuesta, Shlosman & Heller 2006), but our examples show that X-features can appear also in weak bars in low mass galaxies. The weakest X-shapes in our sample appear in NGC 5145, and in the two low mass galaxies IC 3806 and IC 0335 (see Fig. 14), having masses of $\log(M^*/M_\odot) = 9.49$ and $\log(M^*/M_\odot) = 9.94$, respectively. In IC 3806 and NGC 4145 the X-shape appears mainly as four blops in the four corners of the X-feature. All three galaxies can be considered as bulgeless (i.e have no photometric bulge). NGC 5145 has a shallow flux concentration in the surface brightness profile, but it is actually an inner disk in the disk plane. In the unsharp mask images we identify X-shape features also in a few strongly interacting galaxies (NGC 3227 and NGC 4302), in a warped galaxy (NGC 660), and in some otherwise peculiar galaxies (NGC 3190, NGC 3628).

We have six galaxies in our sample, which have a barlens in the classification by Buta et al. (2015), and in which galaxies an X-shape feature is identified in our unsharp mask image. These galaxies are NGC 3185, NGC 3380, NGC 4902, NGC 5957, NGC 7421, and IC 1067 (IC 1067 is shown in Fig. 15). These are naturally also galaxies which appear in the overlapping inclination region of $i \sim 45° - 60°$, where galaxies exhibit both barlenses and X-shape features. The most face-on of these galaxies are NGC 3185 and IC 1067 with i = 38° and 49°, respectively.

8. Morphology of unbarred galaxies

Unbarred galaxies in our sample were selected based on their inner surface brightness profiles, which resemble those of barlens and X-shaped galaxies as much as possible. As an example we show a pair NGC 3599 (unbarred) / NGC 4643 (bl) in Figure 16. Both galaxies have a prominent central peak within 7 – 10", and an exponential sub-section outside that region. In NGC

4643 this sub-section at r ∼ 30" corresponds to the barlens, and in NGC 3599 a similar sub-section extends to r ∼ 20". In NGC 4643 the longer and more elongated part of the bar, ie. the "thin bar", is manifested as a bump in the surface brightness profile at r ∼ 50", which bump is naturally lacking in the unbarred galaxy. More examples of the unbarred galaxies are shown in Figure 17. All these galaxies have sub-structure in the unsharp mask images, and related to their surface brightness profiles, also counterparts among the barlens galaxies can be found. For example, a fairly good correspondence in the surface brightness profiles exists between the unbarred galaxy NGC 3065 (Fig. 17, uppermost panel) and the barlens galaxy NGC 1398 (see Fig. 11, barlens group *c*). Both galaxies have prominent central mass concentrations, and a shallower surface brightness profiles immediately outside that peak. Additional wiggles in the surface brightness profile of NGC 1398 are due to an inner ring and spiral arms.

We have used the surface brightness profiles of the unbarred galaxies to estimate the sizes of the regions corresponding the structures associated to barlenses in barred galaxies. In some galaxies this is the radius defining the photometric bulge (ie. flux above the exponential disk; NGC 4489), whereas in some galaxies it is the exponential sub-section outside the central peak (NGC 3599). These radial distances are marked with dotted vertical lines in Figures 16 and 17.

While deciding where to put that radius we inspected the original and unsharp mask images, in order to recognize the morphological structures behind these profiles. The sizes of these "bulges", together with the sizes of barlenses are plotted as a function of galaxy mass in Figure 18. It appears that the sizes of "bulges" in the unbarred galaxies follow a similar relation as the sizes of barlenses. The number of the unbarred galaxies in the figure is smaller than the total number of unbarred galaxies in our sample, because the radius of the "bulge" was measured only for those galaxies in which it was possible to define it in a reliable manner.

In order to further study the nature of "bulges" of the unbarred galaxies we looked at possible fine-structures in their unsharp mask images. Indeed, many kind of faint features can be recognized. For example, IC 2764 (Fig. 17) shows three blops at r ∼ 12", which is also the radius where the nearly exponential sub-section of the surface brightness profile ends. Characteristic for NGC 4489 and NGC 3599 (Fig. 17) is that both galaxies have weak two-armed spiral-like features inside the exponential sub-sections at r ∼ 12" and 22", respectively. In NGC 5311 (not shown) spiral features appear inside r ∼ 22", which also marks the size of the nuclear lens in the classification by Buta et al. (2015). Also, in IC 5267 (Fig. 17) an elongated feature appears at r = 10" – 15". All the above galaxies have low inclinations of i = 23° - 35°. It is unlikely that the faint features discussed above could form part of a dynamically hot spheroidal component, ie. a classical bulge.

9. Discussion

It is widely accepted that the vertically thick B/P structures are common in the edge-on galaxies (Lütticke, Dettmar & Pohlen 2000; see also the review by Laurikainen & Salo 2016), appearing in ∼2/3 of the S0-Sd galaxies in the nearby universe. Many of them show also X-shape features in unsharp mask images (Bureau et al. 2006) confirming the bar-like origin of these structures. However, the photometric bulges of barred galaxies in less inclined galaxies are repeatedly interpreted as classical bulges. Echoing Kormendy & Barentine (2010): "as long as face-on and edge-on galaxies appear to show physical differences we cannot be sure that we understand them". As a possible solution to this ambiguity it has been suggested by us that the bulges in barred Milky Way mass galaxies are actually the face-on counterparts of B/P bulges (L+2014; A+2015). Taking this view would considerably change the paradigm of bulge formation in the Milky Way mass galaxies. However, before such a view can be adopted, a more in-depth understanding of the properties of these features is needed.

9.1. What are barlenses?

Barlenses have been recognized as lens-like structures embedded in bars in low and moderately inclined galaxies, covering nearly half of the bar size (Laurikainen et al. 2011). The given name was somewhat unfortunate because barlenses were actually assumed to be vertically thick, in a similar manner as the B/P bulges in the edge-on view. This has lead to some confusion in the literature where barlenses are sometimes considered as structures in the disk plane (see for example Gadotti et al. 2015). Looking at their surface brightness profiles in detail shows that barlenses appear as exponential sub-sections, both along the bar major and minor axis (L+2014, their Fig. 1; A+2015, their Fig. 2; Figs. 11, 12 and 15 in this work). These exponential sub-sections can penetrate into the central regions of the galaxies, but more often additional central flux concentrations also appear. We have shown examples indicating that such central concentrations are characteristic to barlenses, but are generally lacking in the X-shaped bars, which is fundamental to understand the nature of these structures.

Related to this matter is also our finding that only ∼ 24% of the barlenses have boxy isophotes. We have 38 galaxies in common with the sample by ED2013 who discussed boxy bar isophotes at intermediate galaxy inclinations (i > 45°). For 22 of these galaxies they find evidence of boxy isophotes, based on similar isophotal analysis as carried out by us. ED2013 interpret this as evidence of B/P bulges. We identify an X-shape feature in 14 of these galaxies (ie. 64% of the B/Ps by ED2013). For the remaining 8 galaxies we confirm the boxy isophotes. In 16 of the galaxies common with our sample ED2013 did not find any evidence of boxiness, in agreement with our analysis (except for NGC 3489 for which galaxy we find boxy isophotes).

It appears that boxy isophotes at i > 45° is an efficient tool to find the vertically thick inner bar components, which at these galaxy inclinations are manifested as X-shape features. However, most barlenses, which typically appear at lower galaxy inclinations, do not exhibit boxy isophotes.

9.2. Barlenses form only in centrally concentrated galaxies

Barlenses have been studied already before they were called as such. In Laurikainen et al. (2007) they were called as lenses, which in the structural decompositions were fitted with a separate function (usually in addition to the main bar component). In Fourier analysis the same structures were manifested as flat or double peaked in the m = 2 density amplitude profiles. The resemblance of such profiles with the simulation models by Athanassoula & Misioritis (2002) made the authors to suggest that those "lenses" might actually be vertically thick inner bar components. That barlenses indeed can be vertically thick was later shown by L+2014 and A+2015. In the first paper the observed axial ratio distribution of the galactic disks in the combined sample of the parent galaxies of barlenses and X-shape features was shown to be flat, as expected if they are the same

features seen at different viewing angles. Athanassoula et al. (2015) showed the connection between barlenses and B/Ps using hydrodynamical simulations. They looked at the vertically thick inner bar components at face-on view, and compared the surface brightness profiles of the model snap-shots with those seen in the observations. In the simulation models the same size was measured for the barlens in the face-on view, and for the X-shape feature in the edge-on view. Consistent with this picture is also the fact that even 88% of the B/P bulges in in edge-on view show X-shape features in the unsharp mask images (Bureau et al. 2006). However, it still remained a puzzle why barlenses appear in earlier Hubble types than the X-shape features. This is shown even more clearly in our Figure 19 (middle panel) using the same inclination bin for both type of objects. In this study we further showed that barlenses appear systematically larger than the X-shape features, in the same galaxy inclination bin (see Figure 10).

These apparent ambiguities can be understood due to the orientations effects, and by the fact that barlenses form mainly in galaxies with peaked central mass concentrations. Salo & Laurikainen (2016) showed that a steep rotation curve is needed to make a barlens morphology in face-on view, while a more shallow rotation curve may lead to boxy or even X-shaped face-on morphology. In principle such central mass concentrations can be associated to classical bulges or other central mass concentrations, which are more pronounced in the early-type galaxies where barlenses generally appear. With our simulation models the effect of the central mass concentration on the bar morphology is illustrated in Figure 20: shown are five models from Salo & Laurikainen (2016) with increasing relative mass, which varies between B/D = 0.01 and 0.16. The models are shown at different galaxy inclinations (keeping the azimuthal angle fixed to $\phi = 90°$). It appears that in the face-on view the barlens morphology becomes increasingly evident when the bulge dominance increases. We can also see that the galaxy inclination where the barlens becomes evident depends on B/D: with large B/D the barlens is visible even at fairly high galaxy inclinations, whereas with low B/D it can be seen only in nearly face-on view. Note that the effective radius of the bulge is fixed to the same value in all these models, being less than 10% of the barlens radius: thus the direct contribution of the bulge flux to the apparent barlens morphology is insignificant.

Further observational evidence for our interpretation can be found from the bulge-disk-bar decompositions made for the S^4G sample by Salo et al. (2015). In Figure 19 shown separately are the galaxies with barlenses and X-shape features: it appears that barlens galaxies indeed are more centrally concentrated (right panel), in spite of the fact that they are not more massive than the galaxies with X-shaped bars (left panel). The comparison is made within an inclination bin $i = 45° - 60°$ where both features appear. Note that although in these decompositions even 4 components were used, the inner bar components were not fitted separately. More sophisticated decompositions were made by L+2014, who used a sample of 29 galaxies, fitting besides bars, bulges and disks, also the inner bar component (bl or X), with a separate function. They found that most of the photometric bulge actually consists of barlenses or X-shape features having <B(X-feature)/T)> = 0.08±0.02 and <B(barlens)/T> = 0.18±0.11. For the central peaks they found B/T = 0.08±0.01 and 0.12±0.02 for the X-shapes and barlenses, respectively (the original paper has less decimals). These values are not far from those used in our simulation models with B/D = 0.01 and 0.08 (ie. B/T = 0.01 and 0.09, respectively). Again, this comparison qualitatively shows that barlenses have at least slightly higher central flux concentrations than the X-shaped bars.

Morphology of the Milky Way (Hubble type T = 3) bar/bulge, showing an X-shape in nearly end-on view ($\phi \sim 30°$), has been reconstructed by Wegg, Gerhard & Portail (2015), based on the best-fitting star count model in the near-IR. More recently the X-shape has been detected also directly by Ness & Lang (2016). Morphology of the Milky Way bulge has been compared with one of the barlens galaxies in our sample, NGC 4314 (T=1), by Bland-Hawthorn & Gerhard (2016; see their Figs. 9 and 10): they suggest that in face-on view the projected bar/bulge of the Milky Way would resemble the barlens morphology of NGC 4314 ($i = 20°$). In the Milky Way the normalized size of the X-feature is 0.3 (a_X/r_{bar} = 1.5/5.0), which is the same as the sizes of the X-shape features in our sample. However, as we are looking at the Milky Way boxy bulge nearly end-on view, it is possible that its relative size is underestimated. Both galaxies have also small inner disks (ie. disky pseudobulges) embedded in the vertically thick inner bar component.

9.3. Optical colors of barlenses

Optical colors of barlenses have been recently studied by HE+2016, and it is interesting to look at if the barlens groups recognized in this study have any association with those colors. HE+2016 used Sloan Digital Sky Survey images (u, g, r, i, z) to study the colors of 43 barlens galaxies. Major and minor axis profiles along the bar were derived using the (g-r) and (i-z) color index maps. They found that barlenses have on average similar colors as the surrounding vertically "thin bars". Barlenses were divided to sub-groups, based on the major axis color profiles. The largest group were those with completely flat color profiles (10/43 galaxies). Interestingly, all these galaxies are early-type systems (7 SO°- SO^{+}, and 3 SO/a). It appears that barlenses of these galaxies have strong "thin bars", ie. they belong to our barlens groups a, b or c. The favorite bar type is a classical rectangular bar (ie. barlens group a). The galaxies with dusty barlenses (8/43) are typically early-type spirals. Prominent nuclear rings appear in 4 of the galaxies: these systems belong either to our barlens group a (N = 1) or b (N = 3), and to our parent galaxy groups 4 or 5. The fractions of inner rings and ringlenses (91-100%, respectively) in these galaxies are exceptionally high. Of the four galaxies that have both a barlens and an X-shape feature, the barlens structure is either dusty (2 galaxies), or has a blue nuclear region (2 galaxies).

One of the messages of this comparison is that the early-type galaxies in our sample, with prominent barlenses, do not have redder central regions (compared to the color of the "thin bar"): if such red central regions (with sizes of barlenses) were seen, that could be interpreted as prominent classical bulges. It is also interesting that barlenses in the early-type spirals can be dusty, in spite of the fact that the mean colors of the barlenses correspond to the colors of typical elliptical galaxies. It means that barlenses are capable of capturing gas and convert that into stars, ie. not all gas is transferred to the nuclear regions of the galaxies. However, colors give us only hints of the mean stellar populations, and spectroscopy is needed to distinguish possible range of stellar ages and metallicities in these structures.

9.4. Individual galaxies with detailed spectroscopy available in the literature

Having in mind that the Milky Way might have a barlens in face-on view, it is worth looking at in which way the stellar populations and kinematics of its bulge have been interpreted in the literature. Recent reviews of the Milky Way bulge are given by Bland-Hawthorn & Gerhard (2016), Di Matteo et al. (2015), Shen & Li (2016), and González & Gadotti (2016). We look at also similar properties of two external galaxies forming part of our barlens galaxy sample, studied in detail in the literature.

Milky Way (MW):

For the Milky Way bulge the early stellar population analysis pointed to a fairly massive classical bulge. The stars of the bulge were found to be metal poor and older than 10 Gyr (Terndrup et al. 1988; Ortolan et al. 1995; Zoccali et al. 2003; Brown et al. 2010). Those stars were also more α-enhanced than the thick disk stars of the same metallicity (McWilliam & Rich 1994; Rich & Origlia 2005; Zoccali et al. 2006; Lecureur et al. 2007; Hill et al. 2011; Johnson et al. 2011). These observations lead to the idea that the Milky Way bulge is a fairly massive classical bulge that formed in a rapid event at high redshift, out of the gas that was not yet enriched by the cycle of star formation and feedback. The idea that the bulge could have been formed via bar buckling episodes was therefore abandoned.

However, this picture has changed more recently. The Milky Way bulge has turned out to have an X-shape morphology (McWilliam & Zoccali 2010; Nataf et al. 2010; Wegg & Gerhard 2013; González et al. 2015). The bulge also rotates cylindrically (Howard et al. 2008; Kunder et al. 2012), as expected for a vertically thick bar component. Nearly 50% of the stellar mass at r < 10 kpc was indeed in place already at high redshift, but the most metal-rich stars ([Fe/H] > -0.4 dex) show a range of stellar ages of 3 – 12 Gyr. The age decreases with increasing metallicity (Bensby et al. 2013; Ness et al. 2014). Such observations are not expected in classical bulges. Although even 60% of the stars in the Milky Way bulge are metal poor, the dynamical models for the bulge do not predict existence of a massive classical bulge (Shen et al. 2010; Di Matteo et al. 2015; see review by Shen & Lin 2016): nowadays the Milky Way bulge is interpreted to largely form part of the bar so that at most 10% of the total galaxy mass belongs to a classical bulge, if at all.

A problem in this interpretation is how to explain the observed age, metallicity, and σ-gradients in the vertical direction (Zoccali et al. 2008; González et al. 2011; Johnson et al. 2011, 2013): the most metal-rich and youngest stars appear at low galactic latitudes, whereas the fraction of dynamically hotter, metal-poor stars (-1<[Fe/H] < -0.5 dex) increases towards higher galactic latitudes. It has been speculated that bar buckling would dilute such stellar population gradients, but they can be explained by assuming that the oldest stars at high galactic latitudes correspond to those originally formed in the thick disk (Ness et al. 2014; Di Matteo 2016). For external galaxies such metallicity gradients in the vertical direction have not much studied yet.

We can compare the observations of the Milky Way bulge with the stellar populations and kinematics of two barlens galaxies, NGC 5701 and NGC 7552, studied by Seidel et al. (2015). The IR-images of these galaxies, their unsharp mask images, and the surface brightness profiles are shown in Figure 21.

NGC 5701 [(R'1)SA<u>B</u>(rl,bl)0/a]:

This galaxy belongs to our barlens group b (Fig. 11) and parent galaxy group 2 (Fig. 13). Integral-field spectroscopy was made by Seidel et al. (2015) using a field-of-view of 36", which covers most of the barlens size having a radius r = 25" in our definition. We use this radius to evaluate the stellar population measurements by Seidel et al. The optical colors are studied by HE+2016: this galaxy shows flat (g-r) and (i-z) color profiles throughout the bar major axis, which colors are also typical for the elliptical galaxies. Using full spectral fitting Seidel et al. find flat (old) age and metallicity profiles in the barlens region (their Fig. 6). Deviations from that appear only in the innermost 4", where nuclear spiral arms reside (Erwin & Sparke 2002), manifested also as a sigma-drop in the same region. Seidel et al. divide the stars also into three sub-populations with different stellar ages (their Fig. 8). It appears that the mass of the barlens is dominated by the old stellar population (70 – 85% of the mass have ages >10 Gyr). However, outside r = 5 – 10" the intermediate age (1.5 – 10 Gyr) stellar population becomes increasingly important towards the edge of the barlens. In the barlens region there is a metallicity gradient: the metallicity goes from solar or slightly sub-solar ([Fe/H]~ 0 – -0.2) from the center to the outer parts. This corresponds to the intermediate metallicities observed in the Milky Way bulge.

NGC 7552 [(R')SB(r<u>s</u>,bl,nr)a)]:

This galaxy belongs to our barlens group d (Fig. 11), and parent galaxy group 5 (Fig. 13). There is a lot of structure in the unsharp mask image in the barlens region at r < 30": a nuclear star forming ring appears at r < 5", and a weak ring-like feature at r~20". These features are manifested also in the stellar populations, metallicities and kinematics, as analyzed by Seidel et al. (2015). The nuclear starburst is dominated by stars younger than 1.5 Gyr, with solar-to-subsolar metallicities. The outer ring-like feature contains a non-negligible amount of old stars (~ 14 Gyr), with lower metallicities than the stars in the inner parts of the galaxy. An important thing is that, although old stars (> 10 Gyr) appear throughout the barlens, the fraction of intermediate age stars (1.5 – 10 Gyr) exceeds that fraction in many regions. Also very young stars (< 1.5 Gyr) appear throughout the barlens. Also in this galaxy a metallicity gradient appears: the metallicities in the barlens region are similar or slightly lower than those in NGC 5701. The rotation curve in the barlens region also shows a double hump, generally associated to B/P bulges.

The interpretation that massive classical bulges appear in external Milky Way mass early-type galaxies has largely based on photometry (bulges have large Sérsic indexes and B/T-values), and on the observation that their stars are on average as old as those in elliptical galaxies. Looking at the mass weighted mean stellar ages of the above two barlens galaxies (excluding the nuclear starburst in NGC 7552), in principle we could make the same conclusion. In NGC 5701 the bulge stars are old also using the light weighted stellar ages. The typical stellar ages of ~10 Gyr or older, are similar as observed in the Milky Way bulge (Sanchez-Blázquez et al. 2011, hereafter SB+2011, and references there). And also, the metallicites of these galaxies are not much different from those of the Milky Way bulge (in NGC 5701 it is slightly higher than in the Milky Way bulge). However, looking at the stellar populations in more detail also shows that both galaxies have a range of stellar ages and metallicity gradients, again similar to those found in the Milky Way bulge. NGC 7552 has also kinematic evidence associating the barlens to a vertically thick bar component.

As in the Milky Way, also in NGC 5701 and NGC 7552 the stellar populations of the barlenses are difficult to interpret by means of classical bulges, inspite of the fact that even 80% (in NGC 5701) and 50% (in NGC 5772) of their stars were formed at high redshifts. In the Milky Way bulge that fraction is ∼60%. In photometric decompositions the values of the Sérsic index and B/T largely depend on how the decompositions are made (see L+2014): low values are obtained when both the "thin bar" and the barlens are fitted with separate functions. That is what actually needs to be done if we are interested in isolating bulges which do not form part of the bar itself.

Kinematic evidence of a B/P bulge has been found also for the barlens galaxy NGC 1640 in our sample by Méndez-Abreu et al. (2014): they used the h_4 coefficient of the Gauss-Hermite parametrization of the line-of-sight velocity distribution, and showed that NGC 1640 has a double minimum before the end of the bar, interpreted as evidence of a vertically thick bar component. Similarly, kinematic evidence of B/P is found by Méndez-Abreu et al. (2008) for NGC 98, which galaxy we would classify as having a barlens (but does not form part of our sample due to its large distance). It appears that detailed stellar population, kinematic, and morphological analysis is needed for more galaxies with barlens and X-shape bars.

9.5. Stellar populations and kinematics in the samples of barred and unbarred galaxies

We can also look at what is known about stellar populations of bulges in major galaxy samples. B/P bulges in the edge-on S0-Sa galaxies has been studied by Williams et al. (2011) and Williams, Bureau & Kuntschner (2012). They found that the main body of the B/P bulges lack a correlation between metallicity gradient and velocity dispersion σ, although such a correlation exists in elliptical galaxies, and is indeed expected in highly relaxed systems. In many studies photometric bulges in the S0-Sbc galaxies are found to be on average old (> 10 Gyr), similar to those in elliptical galaxies (Proctor & Sansom 2002; Falcón-Barroso et al. 2006; McArthur, González & Courteau 2009). Also bars and photometric bulges seem to have similar stellar populations, dominated by old metal-rich stars (Perez et al. 2011, SB+2011). The mass weighted age-gradients are flat at all radii, and the metallicity decreases from the center outwards (Sánchez-Blázquez et al. 2014, hereafter SB+2014). Bulges also have older stars and higher metallicities than the disks (SB+2014), although relatively old stars (age < 4 Gyr) dominate even the disks in spiral galaxies (Morelli et al. 2015). The above stellar population ages of bulges and bars are consistent with the colors obtained for barlenses by HE+2016.

However, as discussed in the previous section, photometric bulges can have also young stellar populations, which is obvious either by comparing the mean mass and light weighted ages, or by dividing the stellar ages into different bins, as was done for example by Seidel et al. (2015). Young stellar ages dominate particularly the bulges of low surface brightness galaxies (Morelli et al. 2012). The stellar populations of bulges in the Calar Alto Legacy Integral Field Spectroscopy Area (CALIFA) survey of ∼ 300 galaxies, covering the redshifts of z = 0.005 – 0.03, and the galaxy mass range of $\log(M^*/M_\odot)$ = 9.1 – 11.8, has been recently analyzed by González-Delgado et al. (2015). They found that the photometric bulges in Sa-Sb galaxies and in the cores of E/S0 galaxies have similar old metal-rich stars. But they also found that the light-weighted mean stellar ages of the bulges in Sa – Sb galaxies are only ∼ 6 Gyr old, compared to ∼ 10 Gyr obtained from the mass weighted stellar ages. It is only in Sc – Scd Hubble types where both the light and mass weighted stellar population ages of bulges are younger than those of the bulges in earlier Hubble types.

Stellar population studies of barred and unbarred galaxies have shown apparent controversial results, but as discussed by Laurikainen & Salo (2016), a critical point is what do we mean by bulge. More metal-rich and α-enhanced bulges in barred galaxies are found by Pérez & Sánchez-Blázquez (2011), who considered as bulges the central regions with similar sizes as nuclear rings. It is well known that the central regions of barlenses have frequently nuclear features (Laurikainen et al. 2011; discussed also in this study): in case of nuclear rings they are star-forming regions, whereas nuclear bars typically have old stellar populations. Therefore, relying on these regions would not tell us anything about the stellar populations of possible spheroidals or B/P bulges of bars. On the other hand, similar stellar populations in barred and unbarred galaxies has been found by SB+2014 for 62 face-on galaxies, and also by Jablonka, Gorgas & Goudfrooij (2007) for 32 edge-on galaxies, without restricting to the innermost regions of bars. These two studies used synthetic stellar population methods in their analysis. It is worth noticing that the above results do not rule out the possibility that bulges in unbarred galaxies were formed in similar processes as the vertically thick inner bar components.

Kinematics of bulges have generally been studied only in small galaxy regions, not yet covering the sizes of barlenses (see a reviews by Falcón-Barroso 2016, and Méndez-Abreu 2016). In Atlas3D (Emsellem et al. 2011; Cappellari et al. 2007) most of the bulges were found to be fast rotating, which is consistent with the idea that they are features of the disk. Only 15% of the bulges in Atlas3D have signatures of B/Ps, in terms of having double humped rotation curves or twisting isophotes (Krajnović et al. 2011). However, while restricting to barlenses and X-shaped structures, as identified in our study, even 36% of the X-shapes and 56% of barlenses in Atlas3D have boxy or twisted isophotes. Most probably the kinematic analysis performed for the Atlas3D has recognized only a small fraction of possible B/P/X-shape bulges in that sample.

Concerning the kinematics of unbarred galaxies, the recent study by Holmes et al. (2015), based on the CALIFA survey, is interesting. They used Hα velocity fields to search for bar-like non-circular flows in barred and unbarred systems. Weakly barred (AB) systems are typically under their detection limit, but in spite of that clear non-circular flows were detected in a few unbarred galaxies, which have no photometric evidence of a bar. These galaxies are not interacting, and have no isophotal twists. Having in mind that only strong amplitudes were detected, most probably only the top of the iceberg was recognized. These photometrically unbarred galaxies could be similar to the unbarred galaxies studied by us. They are not classified as barred, but their photometric bulges might be similar to the inner parts of strong bars, manifested as B/P/X in the edge-on view, and as barlenses in face-on view.

9.6. How relevant is the idea that "bulges" in the Milky Way mass galaxies are largely inner parts of bars?

Above we have discussed that the stars of bulges in the Milky Way mass S0s and early-type spirals in the CALIFA survey (González-Delgado et al. 2015) are older and more metal rich than the stars of their disks. A large majority of the stars in bulges are as old as in the cores of elliptical galaxies. Excluding the nuclear regions bars and bulges also have similar mean stellar population ages and metallicities (SB+2014). Detailed analysis of

some individual barlens galaxies have also shown that the photometric bulges actually have a range of stellar ages between 1.5 – 14 Gyr, which means that the masses of bulges must have been accumulated in a large period of time, or at least more than one starburts event has occurred. In barlens galaxies the photometric bulge consists mostly the barlens itself. Consistent with the idea that bulges were not formed in a single event is also the observation that their mass correlates with the galaxy mass (González-Delgado et al. 2015). When evolved in isolation the central mass concentrations are smaller than in galaxies of clusters, but even in isolated galaxies bulges have old stellar populations (ie. are red in g-i) (Fernández Lorenzo et al. 2006). As bars and photometric bulges are largely made of the same stellar populations, it is possible that bars have played an important role in accumulating the central mass concentrations in galaxies, in some process which rises the stars to higher vertical distances, ie. makes B/P/bl bulges.

What are the stellar populations and metallicities of the formed bulges depends, besides on the formation and evolution of the bar itself, also on possible interaction between the "thin bar" and the thick disk, and on how efficiently the bar collects gas from the surrounding disk. It has been shown by the simulation models that when a barlens forms, a range of stellar population ages appears in the barlens. In the models by Athanassoula, Machado & Rodionov (2013), analyzed by A+2015, barlenses form first in the oldest stellar population, to which mass added later are stars formed from the gas which is gradually accumulated to the bar and the barlens. A different approach was taken by Athanassoula et al. (2016b) who studied mergers of two disk galaxies with hot gaseous halos, ending up to Milky Way mass galaxies with B/T = 0.1 – 0.2 for the classical bulge. The classical bulge formed during a violent relaxation has the oldest stars, while the stars in the barlens are younger and cover a range of stellar ages (7.8 – 8.6 Gyr), which stars were largely formed during the assembling of the disk. Also these simulations are qualitatively consistent with the barlens observations, although the barlenses discussed in our study can have also younger stars, probably related to later gas accretion to these galaxies. However, it is good to have in mind that even based on stellar populations there is no unambiguous way of distinguishing barlenses and classical bulges: namely, also classical bulges formed by wet minor mergers can have young stellar populations, or, old stars in the central regions of bars might appear, originated from the thick disks. Also, although promising, even the above major merger simulations, with relatively small B/T, still have a problem of making too much bulge during the violent relaxation phase (see also the review by Brooks & Christensen 2016).

It is predicted by the cosmological simulation models (de Buhr, Ma & White 2012) that bars which form inside the dark matter halos at z = 1 – 1.3 buckle at z = 0.5 – 0.7, thus forming B/P bulges. These bars are long-lasting and are maintained until z = 0. In principle, earlier bar formation is also possible, but their formation is restricted by large gas fractions observed in high redshift galaxies (gas cannot cool to form stars), and also by a threshold in the relative disk-to-halo mass needed to trigger the disk instability. The epoch predicted for the formation of boxy bulges by de Buhr, Ma & White (2012) is not far away from z∼1, when most of the central mass concentration in galaxies seems to be assembled (van Dokkum et al. 2013). In fact, although the Hubble sequence might be in place at some level already at z = 2.5 (Wuyts et al. 2011), many galaxies at z = 1 – 3 still have irregular clumpy appearance (Abraham et al. 1996; van den Berg et al. 1996; Elmegreen et al. 2007). Based on Fourier analysis of bars it was shown by Salo & Laurikainen (2016), using stacked S^4G density profiles, that the bars with barlenses or X-shape features are mode centrally concentrated than bars in general, indicating that bars and bulges in these galaxies are coupled (see also Díaz-García et al. 2016b for barred and unbarred galaxies).

Using a volume-limited sample it has been shown by Aguerri, Méndez-Abreu & Corsini (2009) that the local galaxy densities of barred and unbarred galaxies are similar, which in our view calls for an explanation for the formation of bulges in unbarred galaxies. Living in similar environments with barred galaxies their formative processes cannot be completely different. In this study we have discussed potential candidates of unbarred galaxies which might have bar-like potential wells. That kind of bar potentials in unbarred galaxies have been discussed from the theoretical point of view by Patsis et al. (2002): those bulges follow similar orbital families as the vertically thick bar components, but are lacking the more extended vertically thin bar components. Indeed, it seems that there is room for the interpretation that most of the bulge mass in the Milky Way mass galaxies actually resides in bars.

10. Summary and conclusions

We use the Spitzer Survey of Stellar Structure in Galaxies (S^4G, Sheth et al. 2010), and the Near-IR S0 galaxy survey (NIRS0S, Laurikainen et al. 2011), to compare the properties of barlenses and X-shape features in the infrared. The sample consists of 88 X-shape features identified in the unsharp mask images, and 85 barlenses that appear in the classifications by Buta et al. (2015) and Laurikainen et al. (2011). Additionally, 41 unbarred galaxies are selected having similar surface brightness profiles with the other galaxies studied by us. The observations are also compared with synthetic images using N-body simulation models.

Unsharp mask images were created for all 214 galaxies, which are used to measure the sizes and ellipticities of the X-shape features, and to inspect the low surface brightness features of bars. For barlenses isophotal analysis is also carried out obtaining the radial profiles of the position angles (PA), ellipticities (ϵ) and B_4 cosine terms. Synthetic images are created using two simulation models taken from Salo & Laurikainen (2016), one representing a bulgeless galaxy (B/D = 0.01), and another where the galaxy had a small bulge (B/D = 0.08) at the beginning of the simulation. The model images are rotated so that a full range of galaxy inclinations in the sky is obtained, which images are measured in a similar manner as the observations. The following results are obtained:

1. Barlenses in the combined S^4G+NIRS0S sample have sizes of $a/r_{bar} \sim 0.5$, confirming the previous result by A+2015 for NIRS0S. We find that the X-shape features appear almost a factor two smaller than barlenses, which is the case even at $i = 45° - 65°$, where both features appear. We show that this size difference is mainly a projection effect, and due to the fact that barlenses form in more centrally concentrated galaxies: observations and simulations show very similar trends, even if in the models the intrinsic sizes of barlenses and X-shape features are the same. Our simulation models with different bulge masses suggest that in order to see an X-shape at $i \lesssim 40°$, the central mass concentration needs to be small. This is consistent with the observation that the X-shape features appear predominantly in galaxies with smaller B/T than the barlenses do.

2. Minor-to-major axis ratios of barlenses appear at b/a = 0.5 – 1.0, in agreement with those given by A+2015 for NIRS0S.

Our analysis further shows that the b/a-distribution for the X-shape features is similar, although not necessarily the same as for barlenses. A comparison with the synthetic images show very similar b/a variations as a function of galaxy inclination.

3. We show that only 24% of barlenses have boxy isophotes, which fraction steadily increases towards higher galaxy inclination. This is shown using the B_4 parameter, which becomes on average negative for $i \gtrsim 50°$. A remarkably similar trend is obtained for the vertically thick bar component in our simulation model with B/D = 0.08. We also verified that the observations of B/P bulges of bars by ED2013 are consistent with this picture. Also, at intermediate galaxy inclinations we find 6 galaxies, which have a barlens in the classification by Buta et al. (2015), and an X-shape feature in our unsharp mask image.

4. Barlenses are divided to morphological sub-groups, based on their fine structures visible in the unsharp mask images. Barlenses can be round featureless structures, or they can have additional low surface brightness features along the bar major axis. Most of the barlenses appear in strong bars of bright galaxies, but they are recognized also in weakly barred galaxies. In fact, our group g, representing the weakest bars among the barlenses in our sample, are morphologically close to unbarred galaxies. Examples of galaxies with X detected in weak bars in low mass galaxies are IC 3806, IC 335 and NGC 5145.

5. The sizes of "bulges" in unbarred galaxies are measured, mimicking the barlens regions of typical barlens galaxies. We find that the sizes of such photometric bulges correlate with the galaxy mass, in a similar manner as the sizes of barlenses. We speculate that such bulges in unbarred galaxies might form in nearly bar-like potentials, as predicted by Patsis et al. (2002).

6. The parent galaxies of barlenses are also divided to subgroups. Characteristic features are inner rings and ringlenses, which appear in 50-100% of the barlens galaxies. The fractions of inner disks (disky pseudobulges) and ansae (at the two ends of the bar) vary among the different parent galaxy groups. Galaxy mass steadily increases from the group 1 to 4, which is also associated to a decreasing fraction of early-type galaxies among these groups. Morphological counterparts of some barlens parent galaxies are identified among the galaxies with X-shaped bars.

Conclusion: we have shown evidence that barlenses at low galaxy inclinations are physically the same inner bar components as B/P/X-shape features in more inclined galaxies. Whether these structures are barlenses or show boxy/peanut/X-shape features depends, besides galaxy orientation, also on the central mass concentration of the parent galaxy. This is shown by comparing directly the properties of barlenses and X-shaped features, and is also verified by our simulation models.

For two barlens galaxies detailed stellar populations and kinematics, given in the literature, are discussed in the context of the identified barlenses. The properties of these galaxies are also compared with those of the Milky Way bulge. We conclude that the stellar populations of barlenses in these galaxies are similar to those of the Milky Way bulge.

Acknowledgements. We acknowledge Panos Patsis of valuable discussions while prepearing this manuscript, and the anonymous referee who's comments have considerable increased the quality of this paper. We also acknowledge the Spitzer Space Telescope of the allocated observing for the S^4G-project, and also of the observing time allocated to NIRS0S project during 2003-2009, based on observations made with several telescopes. They include the New Technology Telescope (NTT), operated at the Southern European Observatory (ESO), William Herschel Telescope (WHT), the Italian Telescopio Nazionale Galileo (TNG), and the Nordic Optical Telescope (NOT), operated on the island of La Palma. This work was also supported by the DAGAL network: Programmme (Marie Curie Actions) of the European Unions Seventh Framework Programme FP7/2007-2013 under REA grant agreement number PITN-GA-2011-289313. We also acknowledge Riku Rautio of participating in making some of the X-shape measurements. All the electgronic figures of this paper are available in a web-page: /www.oulu.fi/astronomy/BLX.

References

Abraham, R., Tanvir, N.R., Santiago, B.X., Ellis, R.S., Glazebrook, K., & van den Berg, S. 1996, MNRAS, 279, 47
Athanassoula, E., & Misioritis, A. 2002, MNRAS, 330, 35
Athanassoula, E. 2005, MNRAS, 358, 1477
Athanassoula, E., Machado, R.E.G., & Rodionov, S.A. 2013, MNRAS, 429, 1949
Athanassoula, E., Laurikainen, E., Salo, H., & Bosma, A. 2015, MNRAS, 454, 3843 (A+2015)
Athanassoula E. in 'Galactic Bulges', Astrophysics and Space Science Library, Volume 418. ISBN 978-3-319-19377-9. Springer International Publishing Switzerland, 2016, p. 391
Athanassoula, E., Rodionov, S.A., Peschen, J.C., & Lambert J.C. 2016, ApJ, 821, 90
Aguerri, J.A.L., Méndez-Abreu, J., & Corsini, E.M. 2009, AA, 495, 491
Beaton, R.L., Majewski, S.R., Guhathakurta, P., Skrutskie, M.F., Cutri, R.M., Good, J., Patterson, R.J., Athanassoula, E., & Bureau, M. 2007, ApJ, 658, 91
Bensby, T., Yee, J.C., Feltzing, S., Johnson, J.A., Gould, A., Cohen, J.G., Asplund, M., Meléndez, J., Lucatello, S., Han, C. et al. 2013, AA, 549, A147
Bland-Hawthorn J., & Gerhard O. 2016, to appear in Ann Rev. Astr. Ap. (arXiv:1602.07702)
Bournaud, F., Daddi, E., Elmegreen, B.G., Elmegreen, D.M., Nesvadba, N., Vanzella, E., Di Matteo, P., Le Tiran, L., Lehnert, M., & Elbaz D. 2008, AA, 486, 741
Bureau, M., Aronica, G., Athanassoula, E., Dettmar, R.-J., Bosma, A., & Freeman, K. C. 2006, MNRAS, 370, 753
Bureau, M., & Freeman, K.C. 1999, AJ, 118, 126
Brown, T.M., Sahu, K., Anderson, J., Tumlinson, J., Valenti, J.A., Smith, E., Jeffery, E.J., Renzini, A., Zoccali, M., & Ferguson, H.C. et al. 2010, ApJ, 725, L19
Brooks, A., & Christensen C. 2016, in 'Galactic Bulges', Astrophysics and Space Science Library, Volume 418. ISBN 978-3-319-19377-9. Springer International Publishing Switzerland, 2016, p. 317
Buta, R.J., Sheth K., Athanassoula, E., Bosma, A., Knapen, J.H., Laurikainen, E., Salo, H., Elmegreen, D., Ho, L.C., Zaritsky, D., et al. 2015, ApJS, 217, 32
Cappellari, M., Emsellem, E., Bacon, R., Bureau, M., Davies, R.L., de Zeeuw, P.T., Falcón-Barroso, J., Krajnović, D., Kuntschner, H., McDermid, R.M. et al. 2007, MNRAS, 379, 418
Chiambur B.C. 2015, ApJ, 810, 120
de Buhr, J., Ma, C-P, & White S. 2015, MNRAS, 426, 983
Díaz-García, S., Salo, H., Laurikainen, E., & Herrera-Endoqui, M. 2016a, AA, 587, 160
Díaz-García, S., Salo, H., & Laurikainen, E. 2016b, accepted to AA
Di Matteo, P. 2016, PASA, doi:10.1017/pas.2016
Di Matteo, P., Gómez, A., Haywood, M., Combes, F., Lehnert, M.D., Ness, M., Snaith, O.N., Katz, D., & Semelin, B. 2015, AA, 577, 1
Emsellem, E., Cappellari, M., Krajnović, D., Alatalo, K., Blitz, L., Bois, M., Bournaud, F., Bureau, M., Davies, R. L., Davis, T.A. et al. 2011, MNRAS, 414, 888
Elmegreen, B.G., Elmegreen, D.M., Knapen, J. H., Buta, R., Block, D. L., & Puerari, I. 2007, ApJ, 670, 97
Elmegreen, B.G., Elmegreen, D.M., Fernandez, M., & Lemonias, J. 2009, AA, 692, 12
Erwin, P., & Debattista, V. 2013, MNRAS, 431, 3060 (ED2013)
Erwin, P., & Sparke, L.S. 2002, AJ, 124, 65
Eskew, M., Zaritsky D., & Meidt, S. 2012, AJ, 143, 139
Falcón-Barroso, J., Bacon, R., Bureau, M., Cappellari, M., Davies, R.L., de Zeeuw, P.T., Emsellem, E., Fathi, K., Krajnović, D., Kuntschner, H. et al. 2006, MNRAS, 369, 529
Fernández Lorenzo, M., Sulentic, J., Verdes-Montenegro, L., Blasco-Herrera, J., Argudo-Fernández, M., Garrido, J., Ramírez-Moreta, P., Ruiz, J. E., Sánchez-Expósito, S., & Santander-Vela, J. D. 2014, ApJ, 788, 39
Gadotti, D., Seidel, M., Sánchez-Blázquez, P., Falcón-Barroso, J., Husemann, B., Coelho, P., & Pérez I. 2015, AA, 584, 90
González, O.A., Rejkuba, M., Zoccali, M., Hill, V., Battaglia, G., Babusiaux, C., Minniti, D., Barbuy, B., Alves-Brito, A., Renzini A., et al. 2011, AA, 530, A54
González, O.A., Zoccali, M., Debattista, V.P., Alonso-García, J., Valenti, E., & Minniti, D. 2015, AA, 583, L5

González O., & Gadotti, D. 2016, in 'Galactic Bulges', Astrophysics and Space Science Library, Volume 418. ISBN 978-3-319-19377-9. Springer International Publishing Switzerland, 2016, p. 199
González-Delgado, R.M., García-Benito, R., Pérez, E., Cid Fernandes, R., de Amorim, A.L., Cortijo-Ferrero, C., Lacerda, E.A.D., López Fernández, R., Vale-Asari, N., Sánchez, S.F. et al. 2015, AA, 581, 103
Herrera-Endoqui, M., Díaz-García, S., Laurikainen, E., & Salo, H. 2015, AA, 582, 86 (HE+2015)
Herrera-Endoqui, M., Salo, H., Laurikainen, E., & Knapen, J. 2016, submitted to AA (HE+2016)
Hill, V., Lecureur, A., Gómez, A., Zoccali, M., Schultheis, M., Babusiaux, C., Royer, F., Barbuy, B., Arenou, F., Minniti, D., & Ortolani, S. 2011, AA, 534, A80
Holmes, L., Spekkens, K., Sánchez, S.F., Walcher, C.J., García-Benito, R., Mast, D., Cortijo-Ferrero, C., Kalinova, V., Marino, R.A., Méndez-Abreu, J., & Barrera-Ballesteros, J.K. 2015, MNRAS, 451, 4397
Hopkins, P., Somerville, R., Cox, T., Hernquist, L., Jogee, S., Keres, D., Ma, C-P., Robertson, B., & Stewart, K. 2009, MNRAS, 397, 802
Howard, C.D., Rich, R.M., Reitzel, D.B., Koch, A., De Propris, R., & Zhao, H. 2008, ApJ, 688, 1060
Iannuzzi, F., & Athanassoula, E. 2015, MNRAS, 450, 2514
Jablonka, P., Gorgas, J., & Goudfrooij, P. 2007, AA, 474, 763
Johnson, C.I., Rich, R.M., Fulbright, J.P., Valenti, E., & McWilliam, A. 2011, ApJ, 732, 108
Johnson, C.I., Rich, R.M., Kobayashi, C., Kunder, A., Pilachowski, C.A., Koch, A., & de Propris, R. 2013, ApJ, 765, 157
Kormendy J., 2016, in 'Galactic Bulges', Astrophysics and Space Science Library, Volume 418. ISBN 978-3-319-19377-9. Springer International Publishing Switzerland, 2016, p. 431
Kormendy, J., & Illingworth, G. 1982, ApJ, 256, 460
Kormendy, J., & Barentine, J.C 2010, ApJ, 715, 176
Krajnović, D., Emsellem, E., Cappellari, M., Alatalo, K., Blitz, L., Bois, M., Bournaud, F., Bureau, M., Davies, R.L., Davis, T.A., et al. 2011, MNRAS, 414, 2923
Kunder, A., Koch, A., Rich, R.M., de Propris, R., Howard, C.D., Stubbs, S.A., Johnson, C.I., Shen, J., Wang, Y., Robin, A.C. et al. 2012, AJ, 143, 57
Laurikainen, E., Salo, H., Buta, R., & Knapen, J. H. 2007, MNRAS, 381, 401
Laurikainen, E., Salo, H., Buta, R., & Knapen, J. H. 2009, ApJ, 692, 34
Laurikainen, E., Salo, H., Buta, R., Knapen, J.H., & Comerón, S. 2010, MNRAS, 405, 1089
Laurikainen, E., Salo, H., Buta, R., & Knapen, J. 2011, MNRAS, 418, 1452
Laurikainen, E., Salo, H., Athanassoula, E., Bosma, A., Buta, R., & Janz, J. 2013, MNRAS, 430, 3489
Laurikainen, E., Salo, H., Athanassoula, E., & Bosma, A. 2014, MNRAS, 444, 80 (L+2014)
Laurikainen, E., & Salo, H. 2016, in 'Galactic Bulges', Astrophysics and Space Science Library, Volume 418. ISBN 978-3-319-19377-9. Springer International Publishing Switzerland, 2016, p. 77 El Laurikainen, R.F. Peletier, D.A. Gadotti, publ. Springer
Lecureur, A., Hill, V., Zoccali, M., Barbuy, B., Gómez, A., Minniti, D., Ortolani, S., & Renzini, A. 2007, AA, 465, 799
Lütticke, R., Dettmar, R.-J., & Pohlen, M. 2000, AAS, 145, 405
Martinez-Valpuesta, I., Shlosman, I., & Heller, C. 2006, ApJ, 637, 214
McArthur, L., González, J., & Courteau, S. 2009, MNRAS, 395, 28
McWilliam, A, & Rich, R.M. 1994, ApJS, 91, 749
McWilliam, A., & Zoccali, M. 2010, ApJ, 724, 1491
Méndez-Abreu, J., Debattista, V. P., Corsini, E. M., & Aguerri, J.A.L. 2014, AA, 572, 25
Méndez-Abreu, J. 2016, in 'Galactic Bulges', Astrophysics and Space Science Library, Volume 418. ISBN 978-3-319-19377-9. Springer International Publishing Switzerland, 2016, p. 15
Mńdez-Abreu, J., Corsini, E. M., Debattista, V.P., De Rijcke, S., Aguerri, J.A.L., & Pizzella, A. 2008, ApJ, 679, 73
Molaeinezhad, A., Falcón-Barroso, J., Martínez-Valpuesta, I., Khosroshahi, H.G., Balcells, M., & Peletier, R.F. 2016, MNRAS, 456, 692
Morelli, L., Corsini, E. M., Pizzella, A., Dalla Bontá, E., Coccato, L., Méndez-Abreu, J., & Cesetti, M. 2012, MNRAS, 423, 962
Morelli, L., Corsini, E. M., Pizzella, A., Dalla Bontá, E., Coccato, L., & Méndez-Abreu, J. 2008 MNRAS, 452, 1128
Muñoz-Mateos, J.C., Sheth, K., Regan, M., Kim, T., Laine J., Erroz-Ferrer, S., Gil de Paz, A., Comerón, S., Hinz, J., Laurikainen, E., et al. 2015, ApJS, 219, 3
Nataf, D.M., Udalski, A., Gould, A., Fouqué, P., & Stanek, K.Z. 2010, ApJ, 721, L28
Ness, M., Debattista, V.P., Bensby, T., Felzing, S., Roskar, R., Cole, D.R., Johnson, J.A., & Freeman, K. 2014, ApJ, 787, L19
Ness, M., & Lang, D. 2016, AJ, 152, 14
Ortolani, S., Renzini, A., Gilmozzi, R., Marconi, G., Barbuy, B., & Bica, R.M. 1995, Nature, 377, 701
Patsis, P. A., Athanassoula, E., Grosbøl, P., & Skokos, Ch. 2002, MNRAS, 335, 1049
Pérez, I., & Sánchez-Blázquez, P. 2011, AA, 529, 64
Portail, M., Wegg, C., Gerhard, O., & Martinez-Valpuesta, I. 2015, MNRAS, 448, 713
Proctor, R.N., & Sansom, A.E. 2002, MNRAS, 333, 517
Querejeta, M., Meidt, S. E., Schinnerer, E., Cisternas, M., Muñoz-Mateos, J-C, Sheth, K., Knapen, J. et al. 2016, ApjS, 219, 5
Rich, R.M., & Origlia, L. 2005, ApJ, 634, 1293
Salo, H., Laurikainen, E., Laine, J., Comerón, S., Gadotti, D.A., Buta, R., Sheth, K., Zaritsky, D., Ho, L., Knapen, J. et al. 2015, ApJS, 219, 4
Salo, H., & Laurikainen, E. 2016, submitted to ApJL
Sánchez-Blázquez, P., Ocvirk, P., Gibson, B.K., Pérez, I., & Peletier, R.F. 2011, MNRAS, 415, 709 (SB+2011)
Sánchez-Blázquez, P., Rosales-Ortega, F.F., Méndez-Abreu, J., Pérez, I., Sánchez, S.F., Zibetti, S., Aguerri, J.A.L., Bland-Hawthorn, J., Catalán-Torrecilla, C., Cid Fernandes, R. et al. 2014, AA, 570, 6 (SB+2014)
Seidel, M.K., Cacho, R., Rioz-Lara, T., Falcón-Barroso, J., Pérez I., Sánchez-Blázquez, P., Vogt, E.P.A., Ness, M., Freeman, K., & Aniyan, S. 2015, MNRAS, 446, 2837
Shen, J., & Li, Z. 2016, in 'Galactic Bulges', Astrophysics and Space Science Library, Volume 418. ISBN 978-3-319-19377-9. Springer International Publishing Switzerland, 2016, p. 233
Sheth, K., Regan, M., Hinz, J.L., Gil de Paz, A., Menéndez-Delmestre, K., Muñoz-Mateos, J.C., Seibert, M., Kim, T., Laurikainen, E., Salo, H., et al. 2010, PASP, 122, 1397
Springel, V., & Hernquist, L. 2005, ApJ 622, L9
Terndrup, D., Elias, J., Gregory, B., Heatcote, S., Phillips, M., Suntzeff, N., & Williams, R. 1988, AJ, 96, 884
van Dokkum, P.G., Leja, J., Nelson, E.J., Patel, S., Skelton, R.E., Momcheva, I., Brammer, G., Whitaker, K.E., Lundgren, B., Fumagalli, M. et al. 2013, ApJ, 771, 35
van den Berg, S., Abraham, R., Ellis, R., Tanvir, N., Santiago, B., & Glazebrook, K. 1996, AL, 112, 359
Wegg, C., & Gerhard, O. 2013, MNRAS, 435, 1874
Wegg, C., Gerhard, O., & Portail, M. 2015, MNRAS, 450, 4050
White, S.D., & Rees, M.J. 1978, MNRAS, 183, 341
Williams, M.J., Zamojski, M.A., Bureau, M., Kuntschner, H., Merrifield, M.R., de Zeeuw, P.T., & Kuijken, K. 2011, MNRAS, 414, 2163
Williams, M.J., Bureau, M., & Kuntschner, H. 2012, MNRAS, 427, 99
Wuyts, S., Förster Schreiber, N.M., van der Wel, A., Magnelli, B., Guo, Y., Genzel, R., Lutz, D., Aussel, H., Barro, G., Berta, S. et al. 2011, ApJ, 742, 96
Zoccali, M., Renzini, A., Ortolani, S., Greggio, L., Saviane, I., Cassisi, S., Rejkuba, M., Barbuy, B., Rich, R.M., & Bica, E. 2003, AA, 399, 931
Zoccali, M., Lecureur, A., Barbuy, B., Hill, V., Renzini, A., Minniti, D., Momany, Y., Gómez, A., & Ortolani, S. 2006, AA, 457, L1
Zoccali, M., Hill, V., Lecureur, A., Barbuy, B., Renzini, A., Minniti, D., Gómez, A., & Ortolani, S. 2008, AA, 486, 177
Yoshino, A., & Yamauchi, C. 2014, MNRAS, 446, 3749

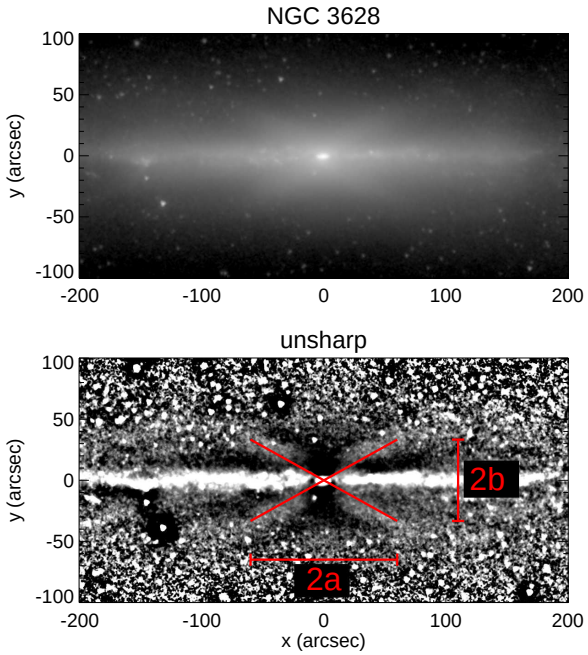


Fig. 1: NGC 3628 (*upper panel*) is used as an example to demonstrate how the sizes of the X-shapes are measured. The unsharp mask image (*lower panel*) is used, which is rotated so that the bar major axis appears horizontally. The extent of the feature is measured both along the bar direction and perpendicular to it, and the semilenghts are denoted by a and b, respectively.

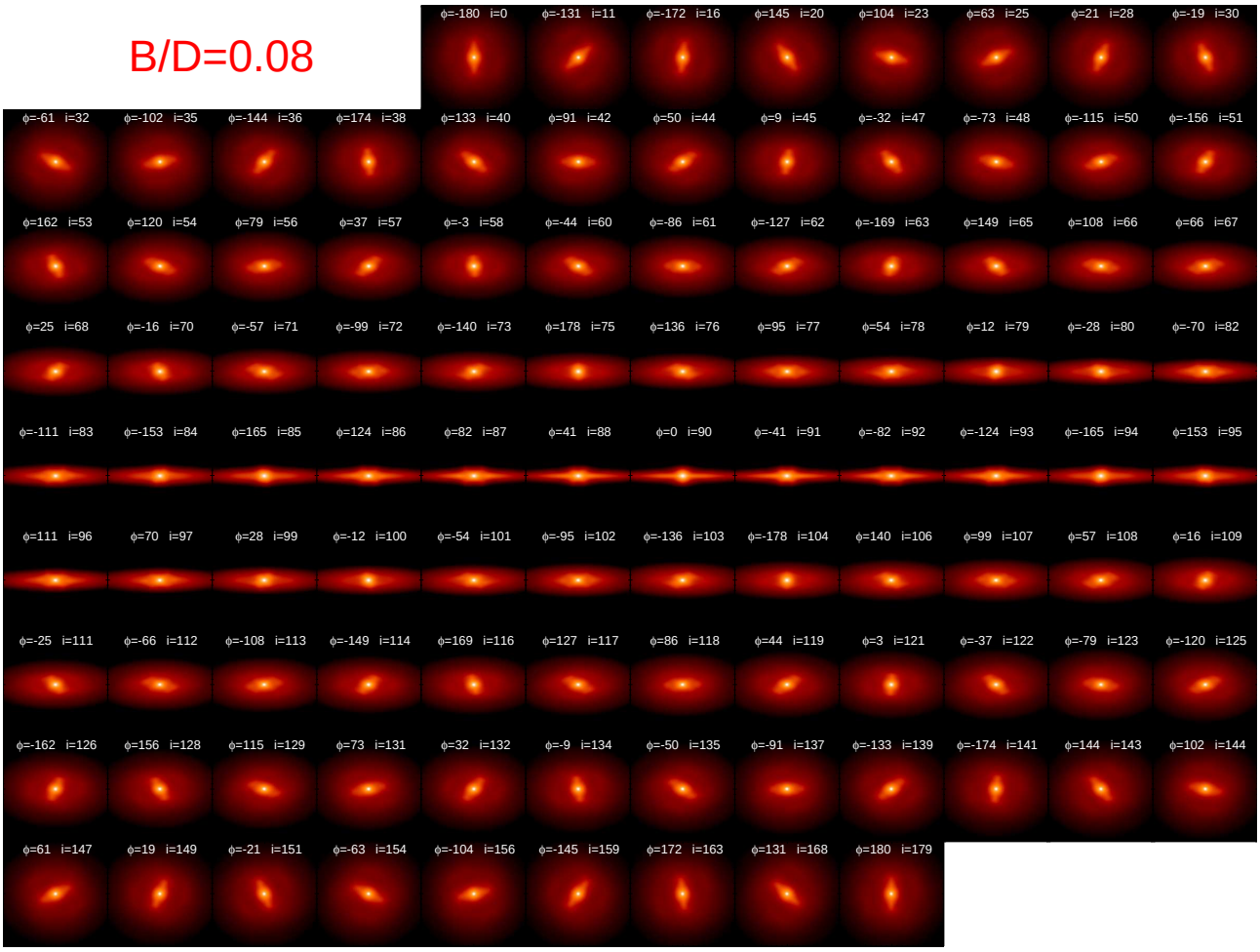
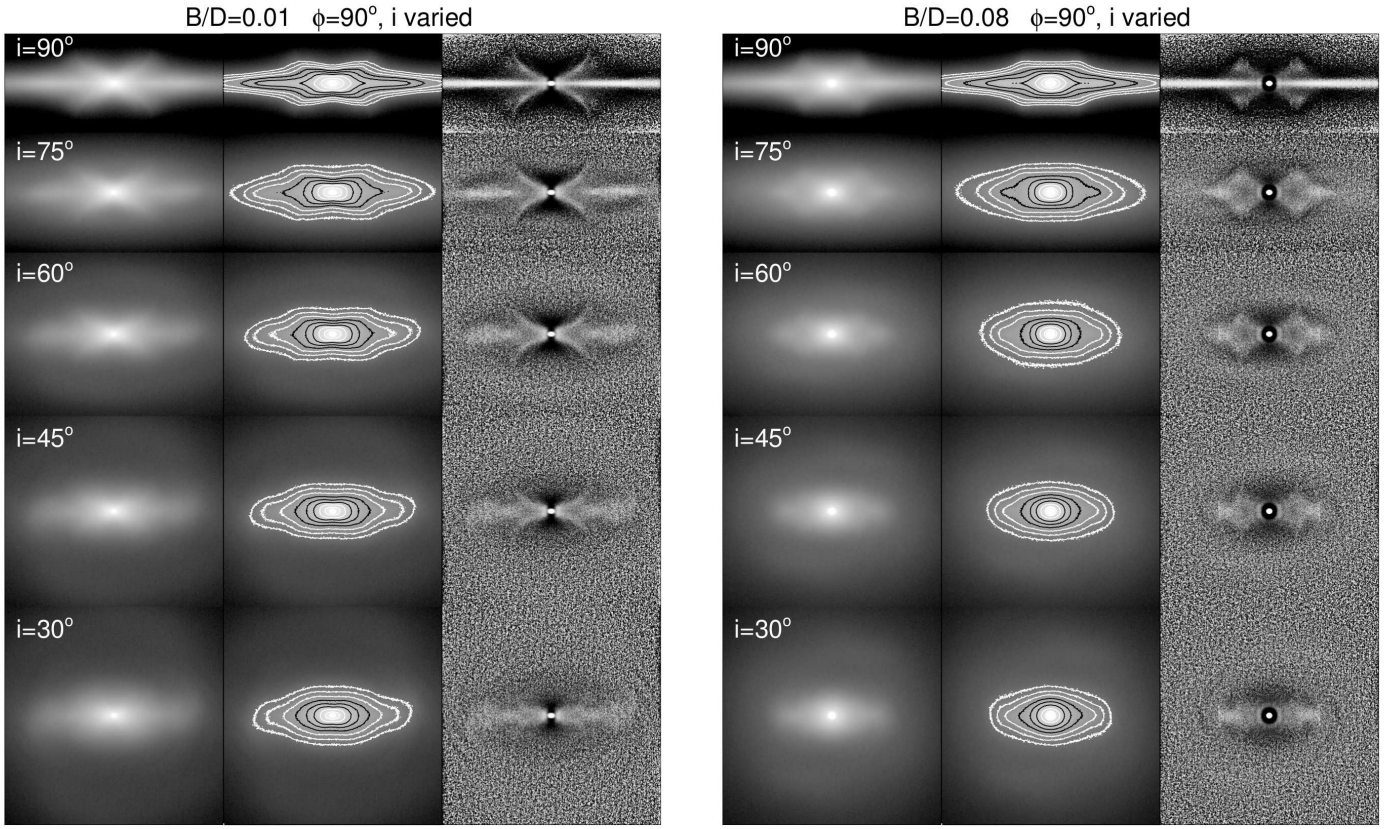
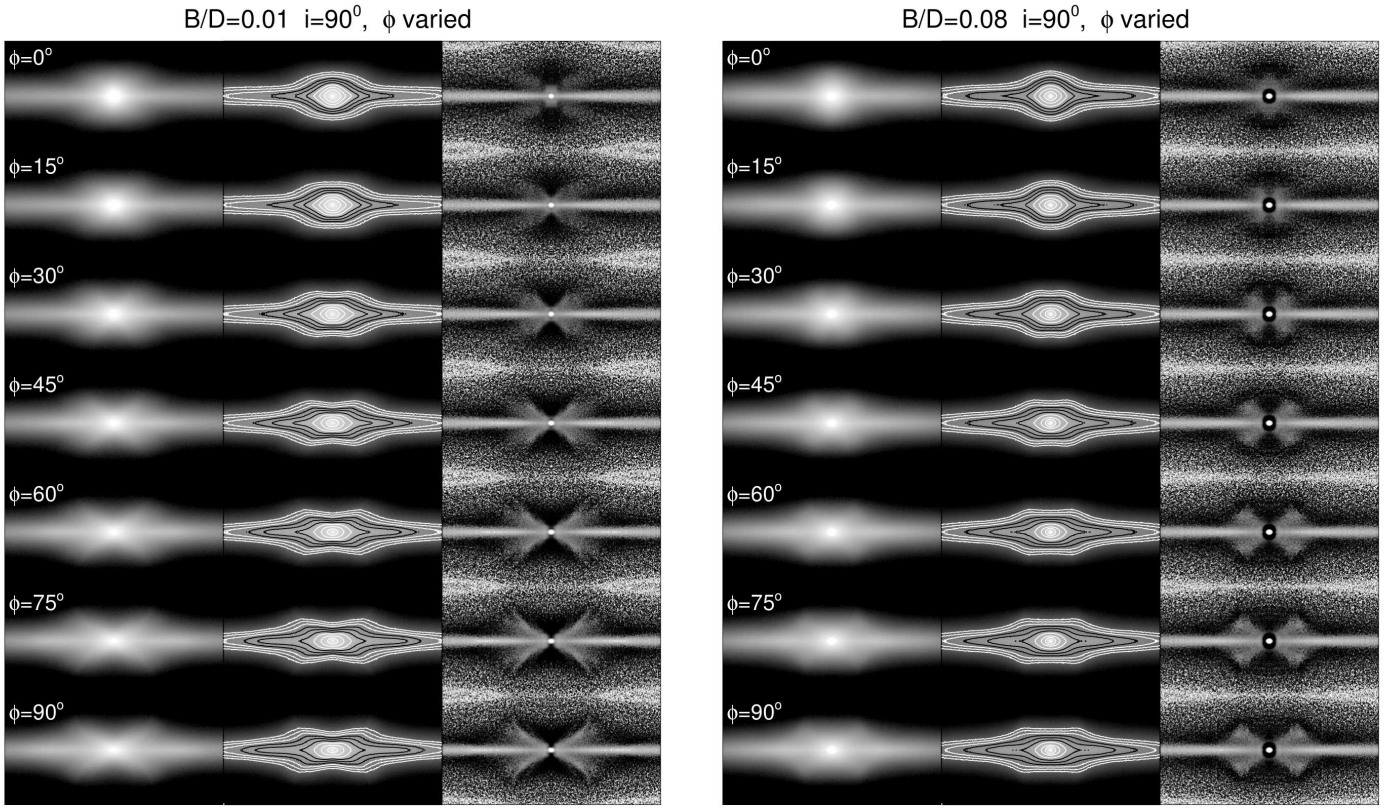


Fig. 2: Synthetic images used in comparison with observations, from the simulation with B/D = 0.08. The same simulation snapshot is viewed from 100 isotropically chosen directions. The labels in the frames indicate the viewing azimuth ϕ with respect to bar major axis, and the viewing inclination i. The line-of-nodes are horizontal. The simulation model is explained in Section 3.3.



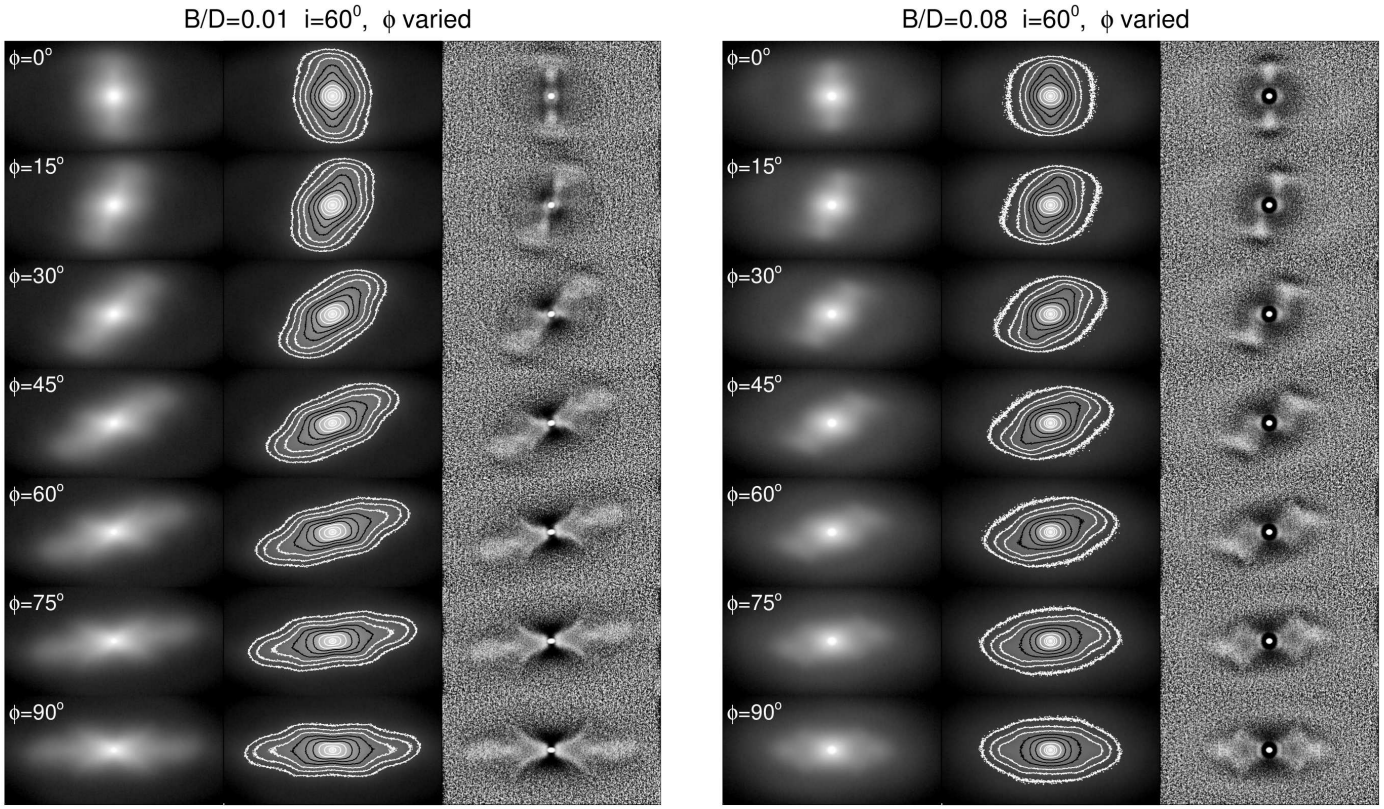
(a) (b)

Fig. 3: Snapshot of the simulation with *(a)* B/D = 0.01 and *(b)* $B/D = 0.08$ are viewed at azimuthal angle $\phi = 90°$, from five galaxy inclinations ($i = 90°$ corresponds the side-on-view of the bar). The line-of-node is horizontal. The left panels show the synthetic images, in the middle panel the isophotal contours, separated by 0.5 mags, are overlayed on the images, while the right panels show the unsharp mask images.



(a) (b)

Fig. 4: Same as Figure 3, except that the inclination is fixed to $i = 90°$, and the viewing azimuth is varied. In the upper panels the bar is seen end-on ($\phi = 0°$), and in the lowest panels side-on ($\phi = 90°$).



(a) (b)

Fig. 5: Same as Figure 4, except that the inclination is fixed to $i = 60°$. In the different panels the azimuthal angle ϕ varies.

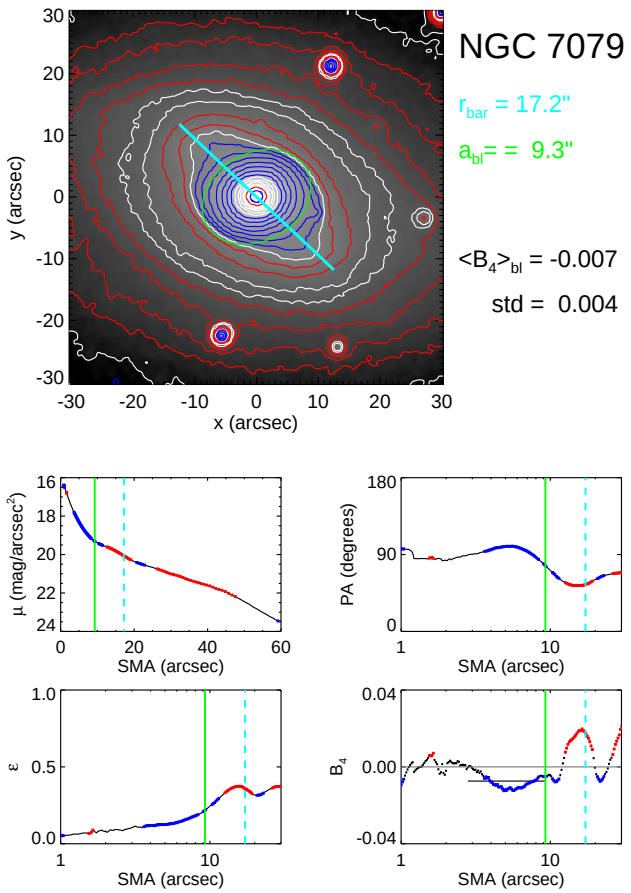


Fig. 6: Isophotal analysis performed for a barlens galaxy NGC 7079. In the upper panel the 3.6 μm image is shown in the sky plane with North up and East left: overlaid are the isophotal contours. The blue line indicates the bar length and orientation, and the green ellipse denotes the ellipse fit to the barlens. The four lower panels show the radial profiles from IRAF ellipse: the surface brightness μ (in mag arcsec^{-2}) *(upper left panel)*, the position angle (PA°) *(upper right panel)*, the ellipticity (ϵ) *(lower left panel)*, and the B_4 parameter *(lower right panel)* as a function of semi-major axis. B_4 is used as proxy for the boxiness: in the small panels the blue and red colors indicate the regions where $B_4 < -0.005$ and $B_4 > 0.005$, respectively. The green vertical full line shows the radius of the barlens, and the dashed blue line the bar radius (same colours are used on the contour plot). The labels in the upper right indicate the bar radius (r_{bar}), the semi-major axis length of the barlens (a_{bl}), the mean and standard deviation of B_4 in the region where the isophotal radius is (0.3 – 1.0) a_{bl}. Similar analysis has been carried out for all 84 barlens galaxies in our sample.

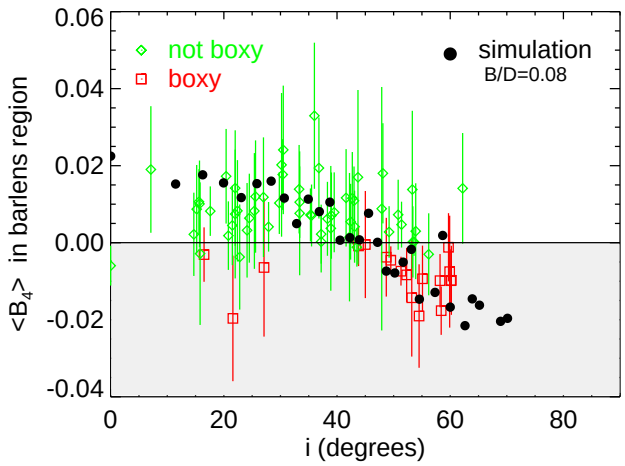


Fig. 7: The mean value of B_4 parameter in the region of the barlens (isophotal radius in range (0.3 – 1.0) a_{bl}) is displayed as a function of galaxy inclination. The red and green symbols indicate galaxies which have been judged boxy and non-boxy, based on visual inspection of the isophotes and the B_4 profiles. The filled circles show the same parameter measured from the synthetic images, for the simulation model with B/D = 0.08. The error bars in the observation points correspond to ± one standard deviation of B_4 in the measurement region.

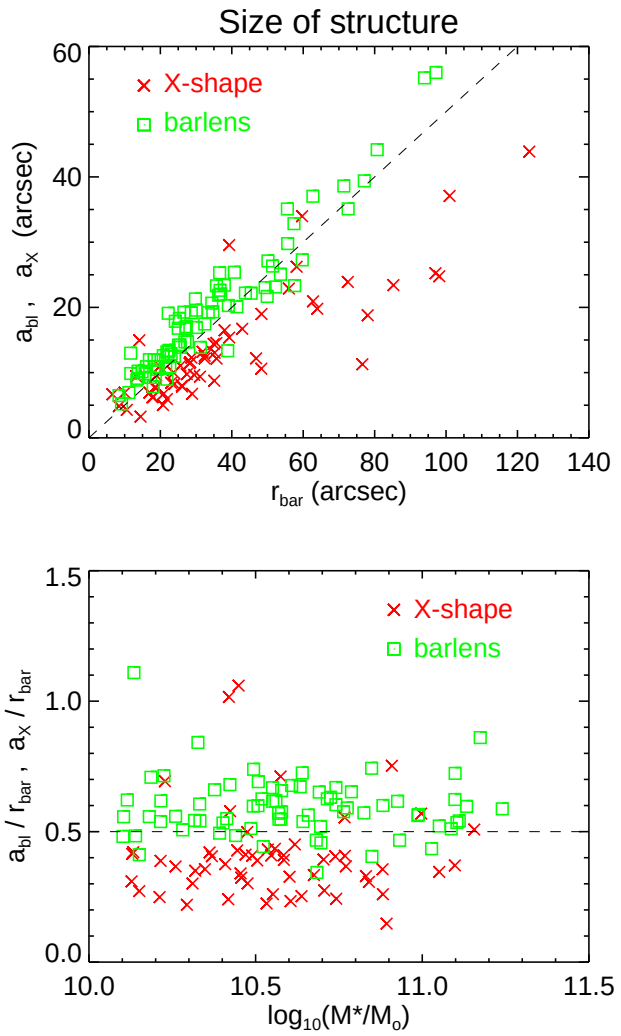


Fig. 8: *Upper panel*: the sizes (a) of barlenses and X-shape features are shown as a function of bar radius (r_{bar}), given in arcseconds. All measurements are in the sky plane. For X-shapes the measurements are from the current study, and for barlenses from Laurikainen et al. (2011) and HE+2016. *Lower panel*: The sizes of barlenses and X-shape features are normalized to the barlength, and drawn as a function of the parent stellar galaxy mass (M*), taken from S^4G Pipeline 3 (Muńoz-Mateos et al., 2015). The measured uncertainties are typically less than 0.5 arcsec.

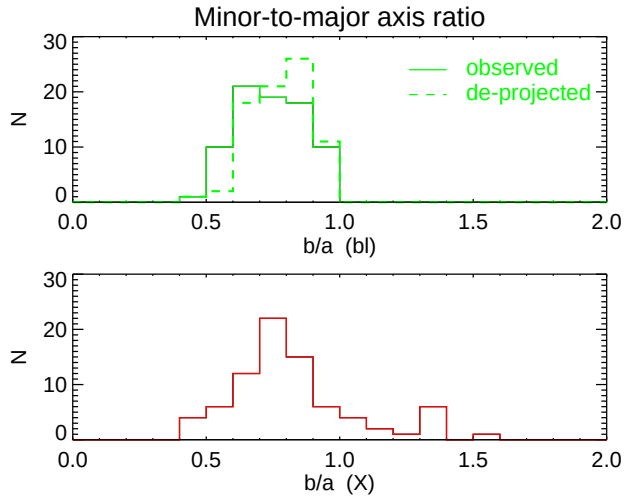


Fig. 9: Distributions of the minor-to-major axis ratios (b/a) of barlenses *(upper panel)*, both as measured in the sky-plane, and after deprojection to disk-plane. The *lower panel* shows the b/a ratio for the X-shapes (in the sky plane).

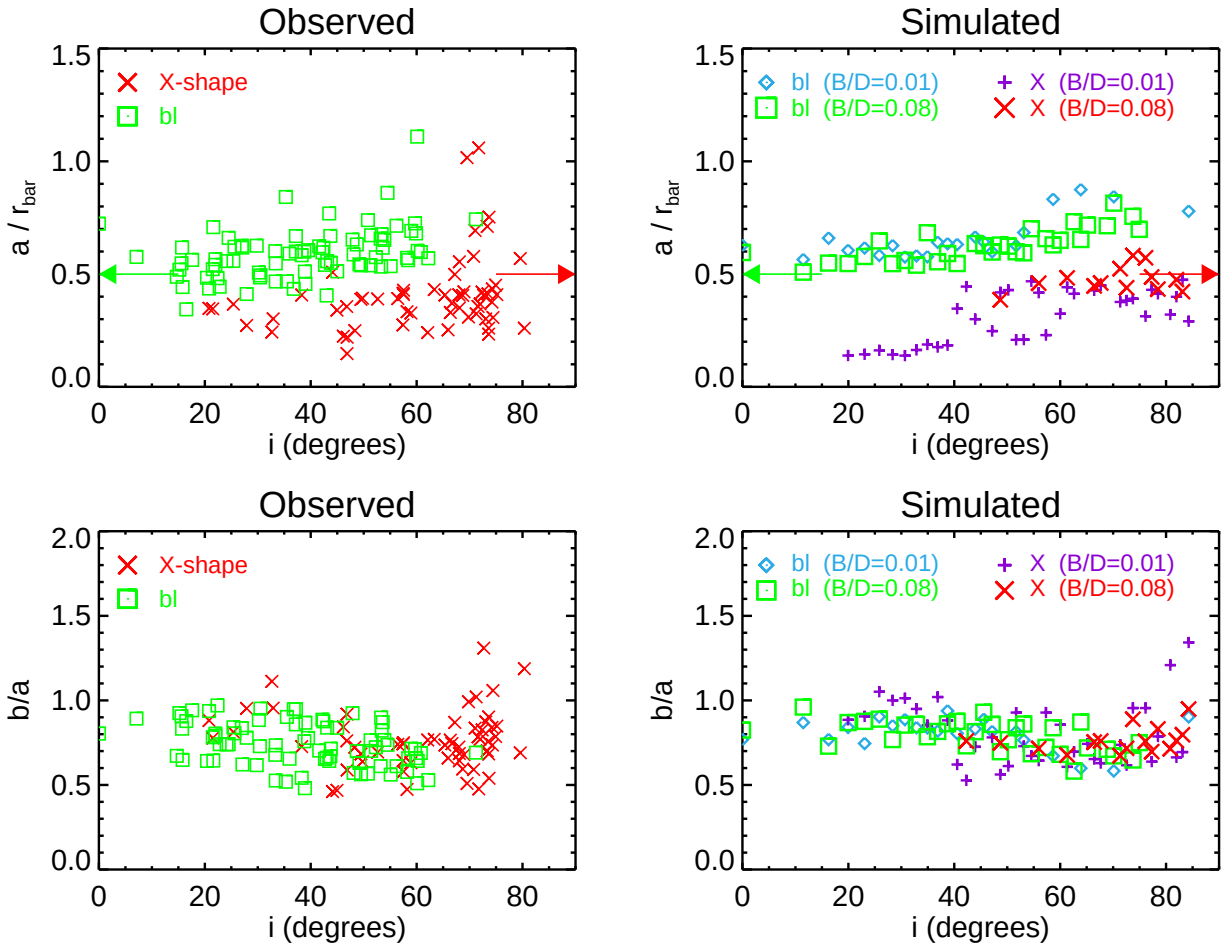


Fig. 10: Normalized sizes (a/r_{bar}) and the minor-to-major axis ratios (b/a) of barlenses and X-shape features of the galaxies are plotted as a function of parent galaxy inclination (*left panels*). The same parameters for the synthetic images are also shown (*right panels*). The simulations with small (B/D = 0.01) and large bulge (B/D = 0.08) are shown with different symbols. The arrows in the two panels use the model with B/D = 0.08, indicating the normalized barlens size in face-on view (green arrow in the left), and the size of the X-shape when seen the same model edge-on (red arrow in the right). The measured uncertainties are typically less than 0.5 arcsec.

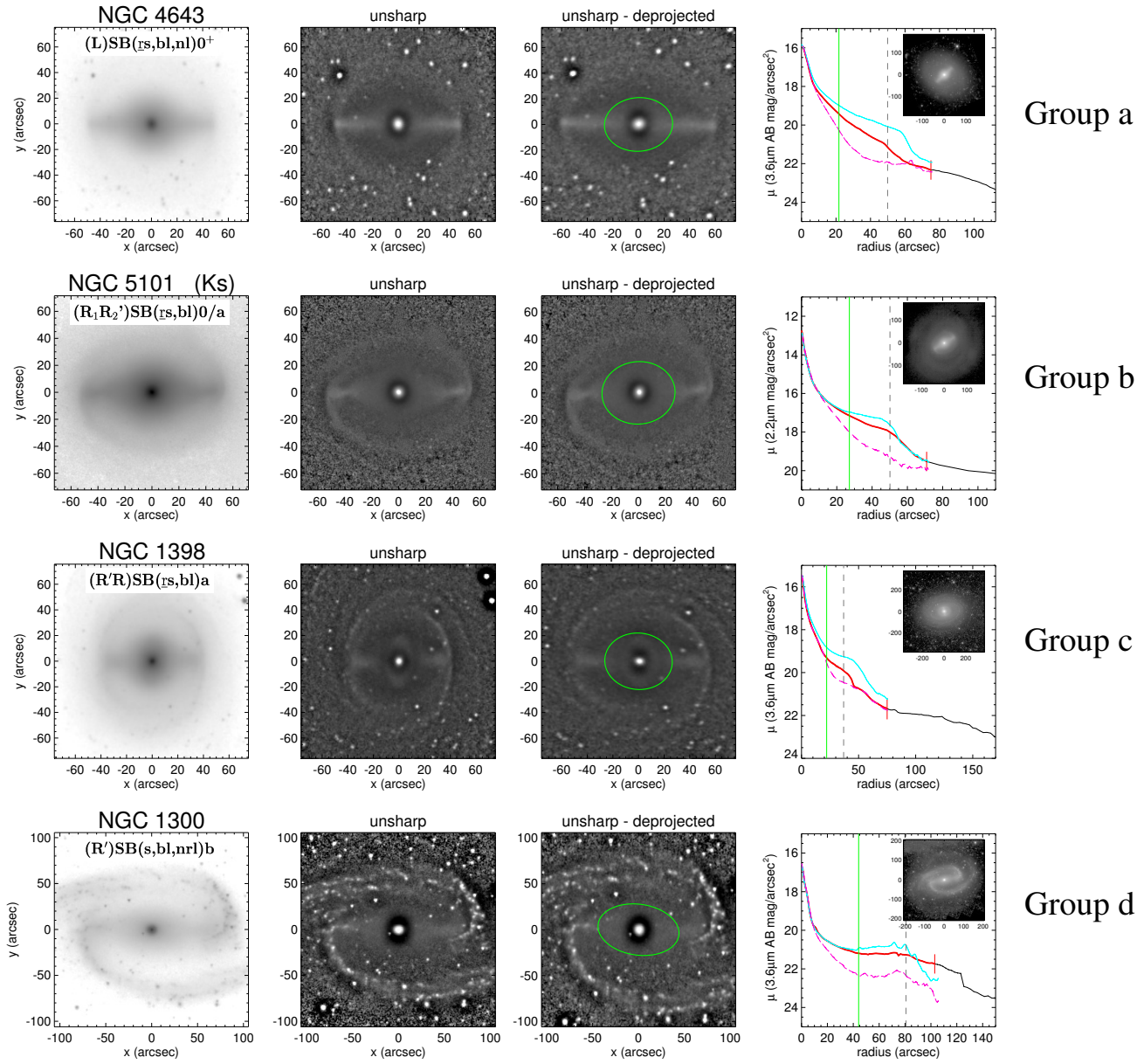


Fig. 11: Barlens groups a, b, c, and d, as explained in Section 6.1. The *left panels* show the 3.6 μm images and the *two middle panels* the observed (left) and deprojected (right) unsharp mask images. The images are cut to show only the bar region, and the bar is always aligned horizontally. The green circles show the barlenses. In the *right panels* the surface brightness profiles are shown. The black lines are the isophotal profiles from IRAF ellipse, and the profiles cuts along the bar major (blue line) and minor axis (red dashed line) are shown separately in the same panel. However, in case that the galaxy inclination is larger than 65° only the major axis profile is shown. The small panels in the upper corners show the images in full size and having original orientations in the sky. The vertical full and dashed lines indicate the sizes of barlenses and bars, respectively. The red portion of the surface brightness profile indicates the range of the unsharp mask image. In case NIRS0S K_s is shown instead of 3.6 μm image, this is indicated in the label of the leftmost frame.

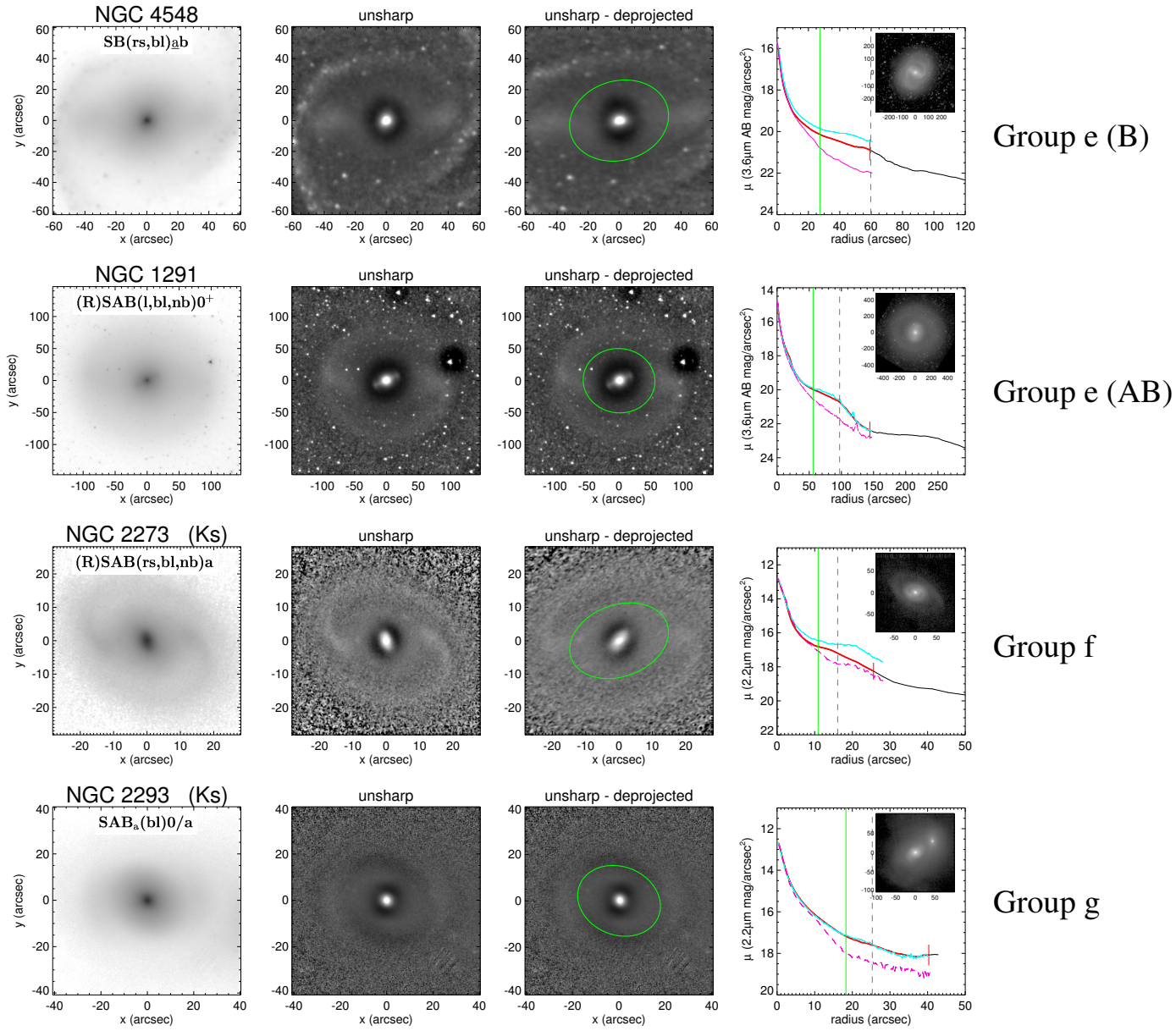
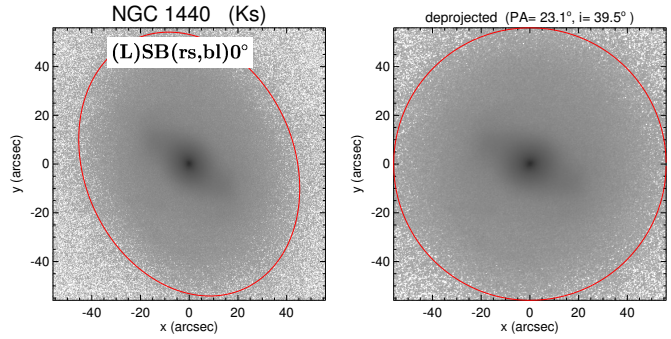
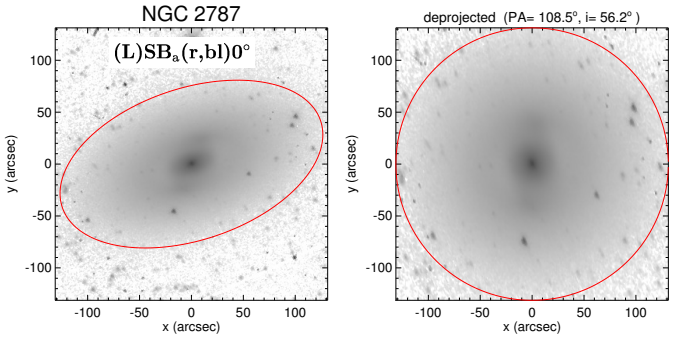


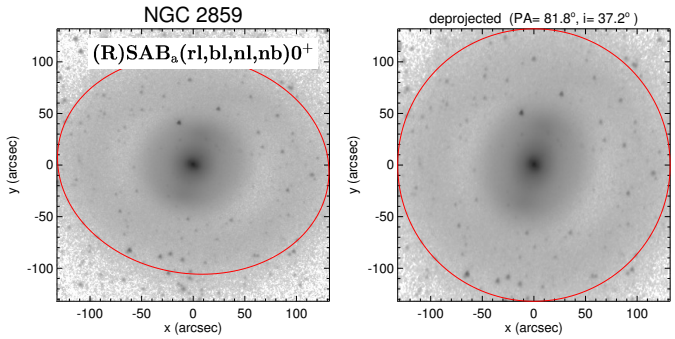
Fig. 12: Barlens groups e, f, and g, as explained in Section 6.1. The format of the figure is the same as in Fig. 11.



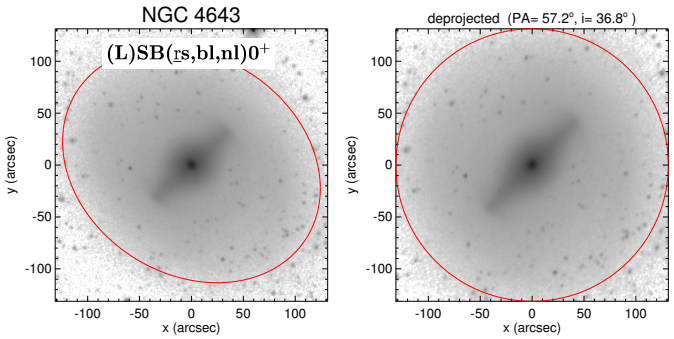
(a) Parent galaxy group 1a



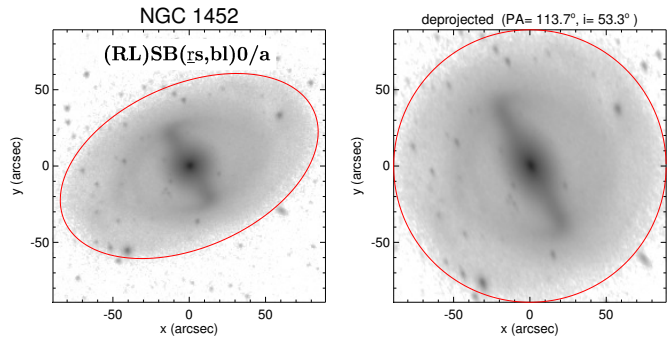
(b) Parent galaxy group 1b



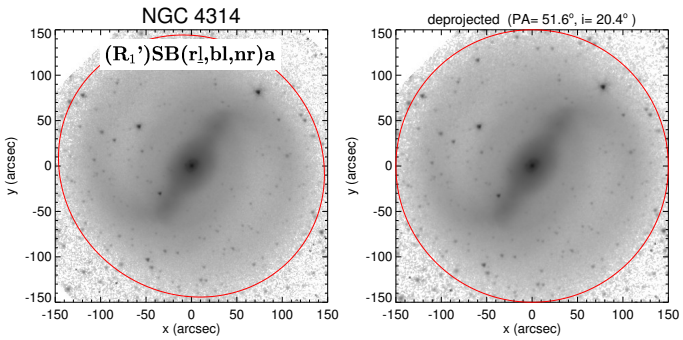
(c) Parent galaxy group 2



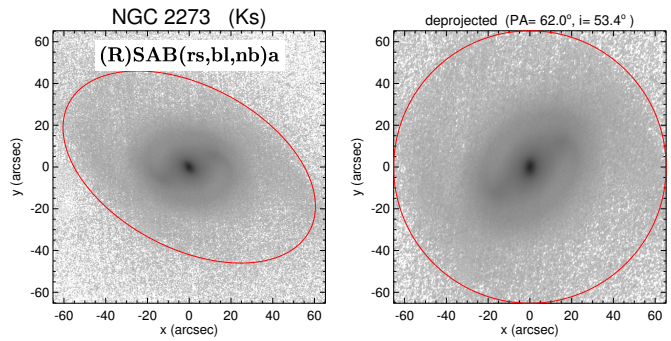
(d) Parent galaxy group 3



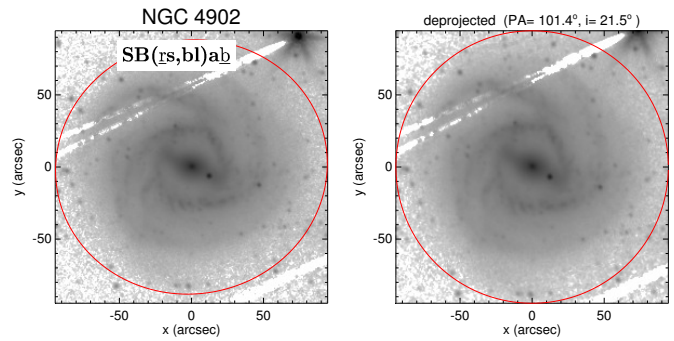
(e) Parent galaxy group 4



(f) Parent galaxy group 5



(g) Parent galaxy group 6



(h) Parent galaxy group 7

Fig. 13: Parent galaxy groups as defined in Section 6.2. The galaxies are shown both in the sky *(left panels)* and when deprojected to disk plane *(right panels)*. The red ellipse indicates the orientation of the outer disk; this corresponds to the circle in the deprojected image. The images are 3.6 μm images, unless indicated by K_s after the galaxy name.

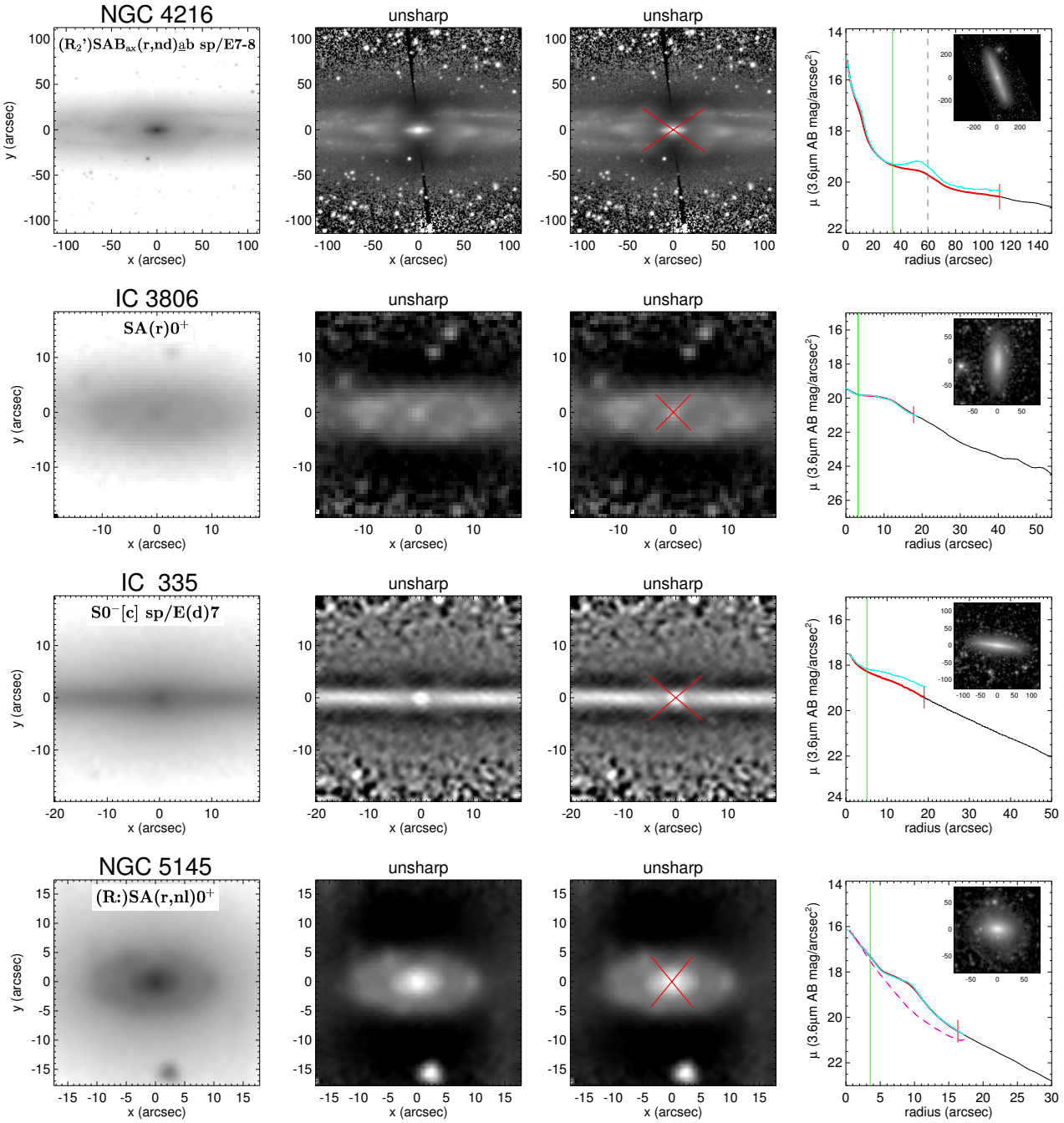


Fig. 14: Four X-shaped galaxies are shown: NGC 4216 has a prominent inner disk. The three other galaxies have the weakest X-shaped features in our sample. They are shown in the same format as Figure 11, except that the deprojected images are not shown. The red cross in the right middle panel shows our measurement of the X-feature.

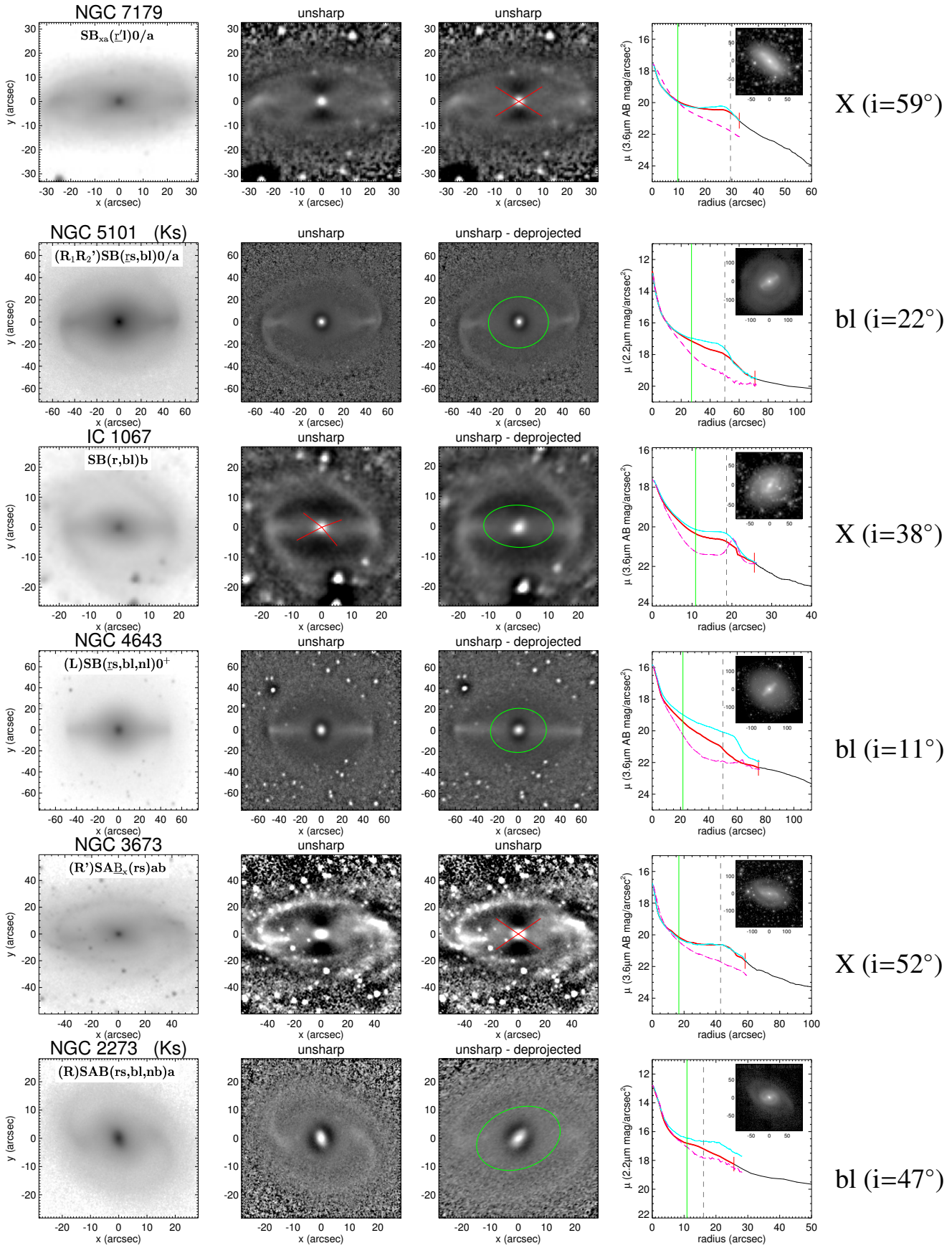


Fig. 15: Three galaxy pairs are shown, in which the parent galaxies of a barlens and an X-shape feature have similar morphologies: NGC 7179 (X) /NGC 5101 (bl), IC 1067 (X) / NGC 4643 (bl), and NGC 3673 (X) / NGC 2273 (bl). Because of large galaxy inclination, the deprojected images for NGC 7179 and NGC 3673 are not shown. IC 1067 has both a barlens and an X-shape feature. The format is the same as in Fig. 11.

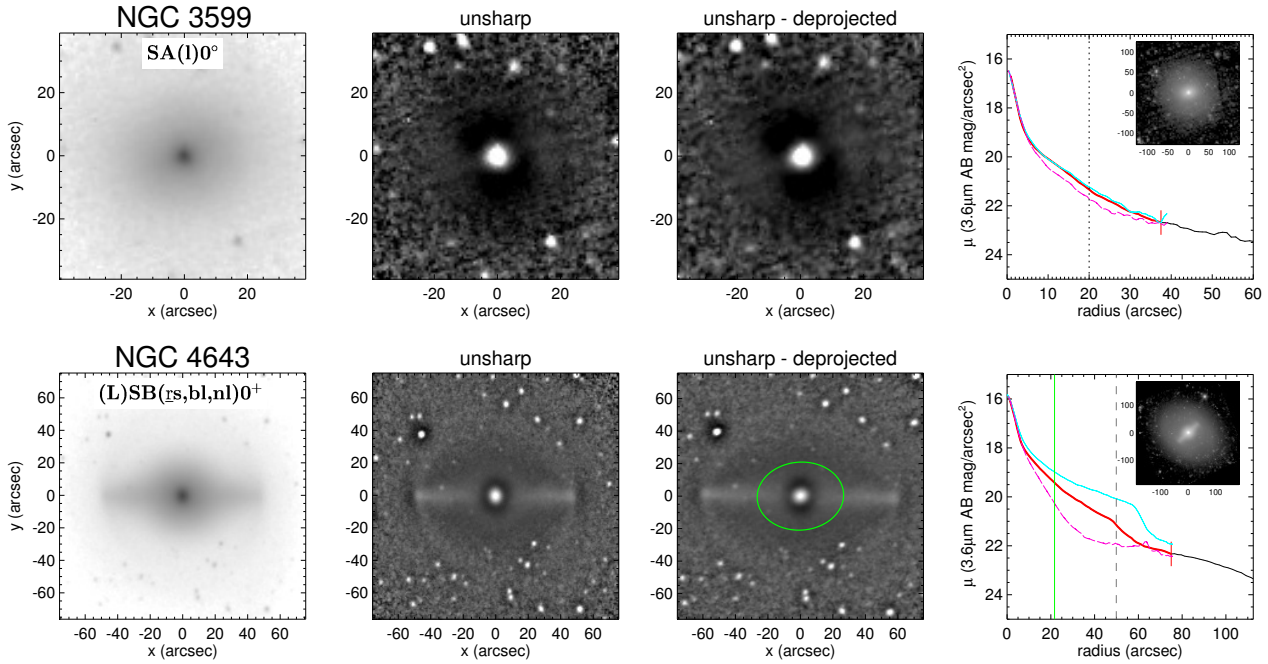


Fig. 16: Our selection criterion for the unbarred galaxies is demonstrated: original images, unsharp mask images, and the surface brightness profiles for a unbarred (NGC 3599) and a barlens (NGC 4643) galaxy are compared. Notice the similar central flux concentrations, and the subsequent, nearly exponential sub-sections in their surface brightness profiles. The dotted vertical line in the profile of NGC 3599 marks the extent of the "barlens-like" structure. The dashed and full vertical lines in the profile of NGC 4643 show the sizes of the barlens and the bar, respectively. The same format is adopted as in Fig. 11.

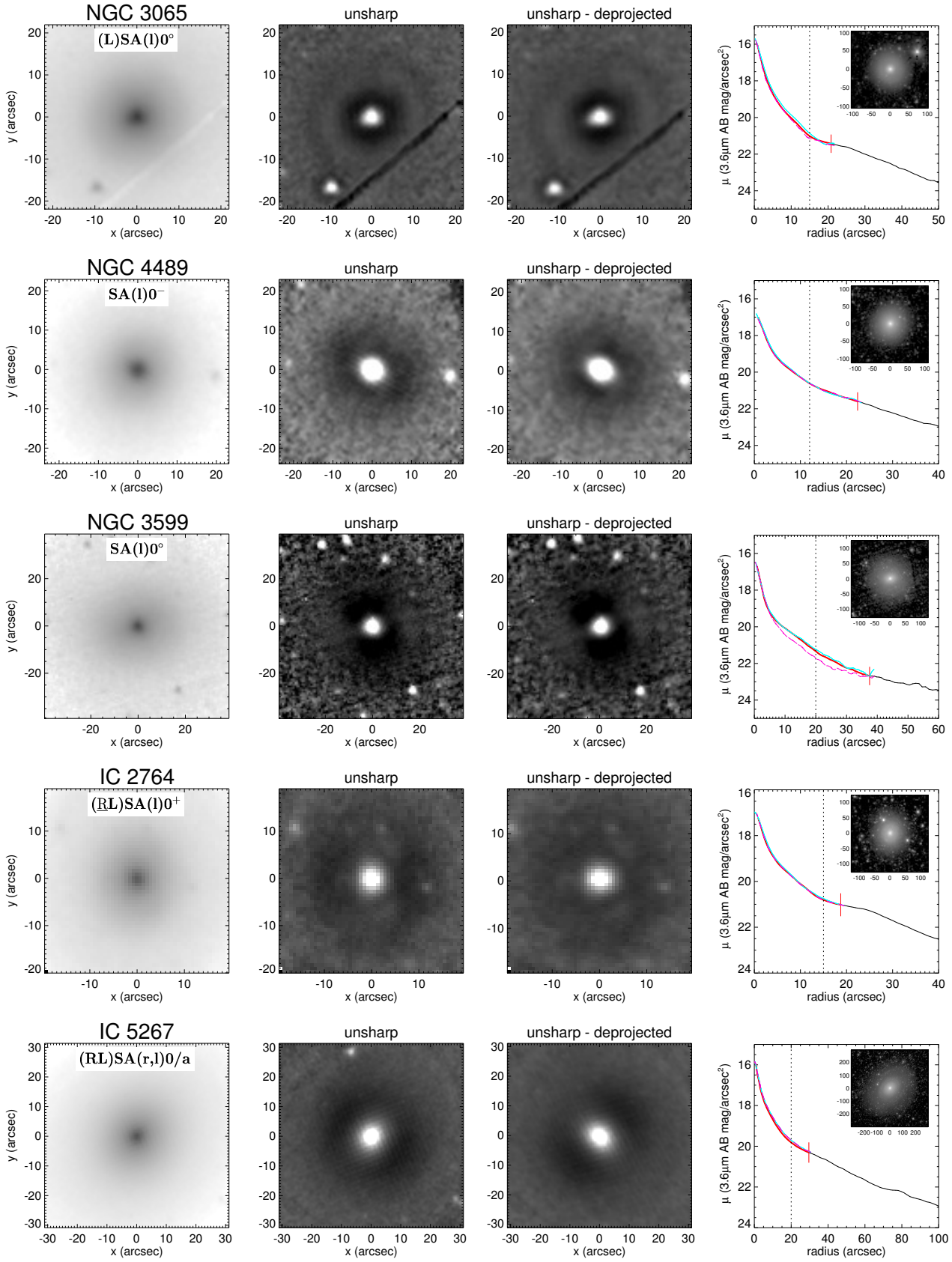


Fig. 17: A selected sub-sample of the unbarred galaxies, representative of the surface brightness profiles and innermost morphologies in the unsharp mask images. The same format is adopted as in Fig. 11. Meaning of the dotted vertical line is the same as in Figure 16.

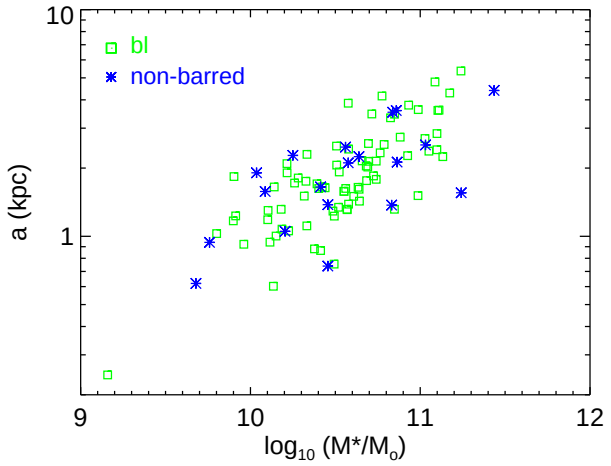


Fig. 18: Sizes of barlenses in barred galaxies (green boxes), and in barlens-like structure components in unbarred galaxies (blue stars), are plotted as a function of galaxy stellar mass (M^*). The semimajor-axis lengths are given in kpc.

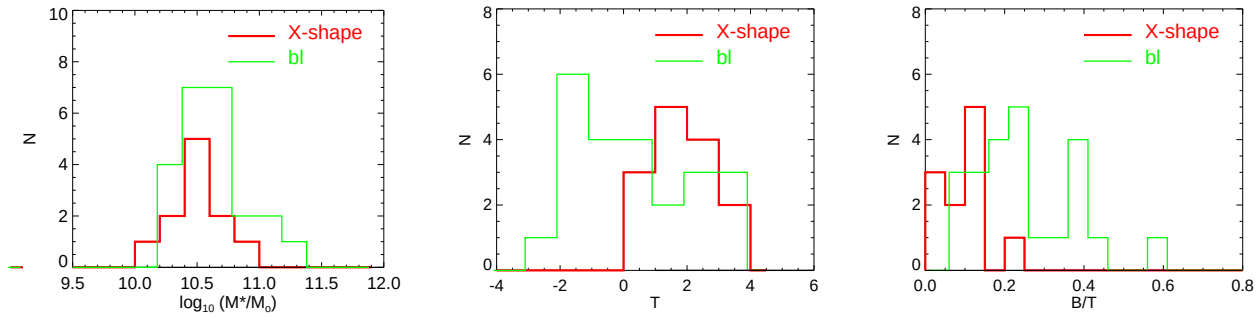


Fig. 19: Number histograms of the parent galaxy stellar masses (M^*), Hubble stages (T), and bulge-to-total flux ratios (B/T, taken from S^4G Pipeline 4, Salo et al. (2015), are shown separately for barlenses and X-shape features in our samples. In this plot shown are only galaxies at $i = 45° - 60°$.

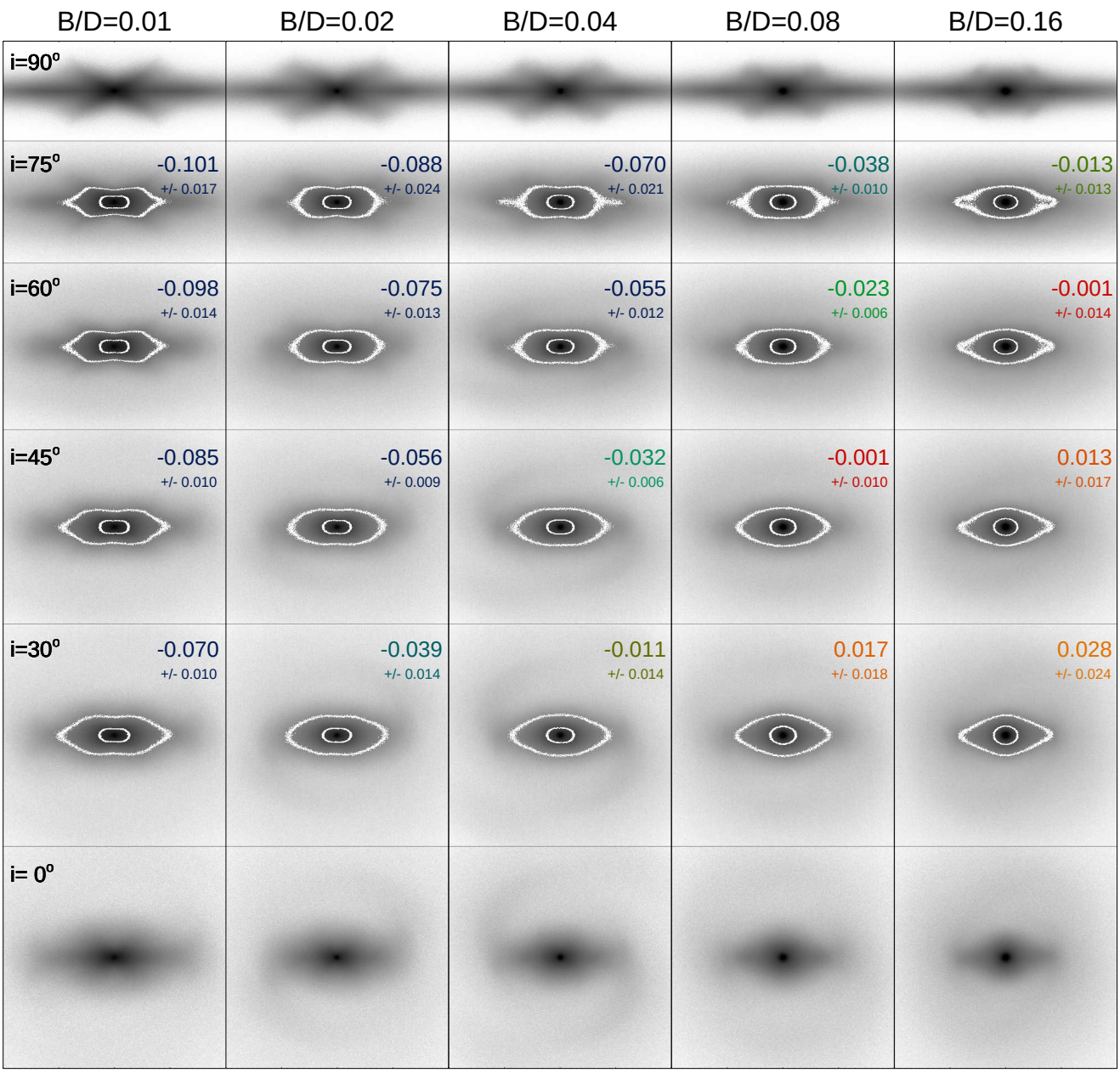


Fig. 20: Five simulation models from Salo & Laurikainen (2016) are shown at five different galaxy inclinations. The models differ in the bulge-to-disk mass ratio which varies from B/D = 0.01 to B/D = 0.16. The labels in the frames for i =30° – 75° indicate the mean and standard deviation of B_4 for the B/P/X/bl feature, measured from the region between the two marked isophotes.

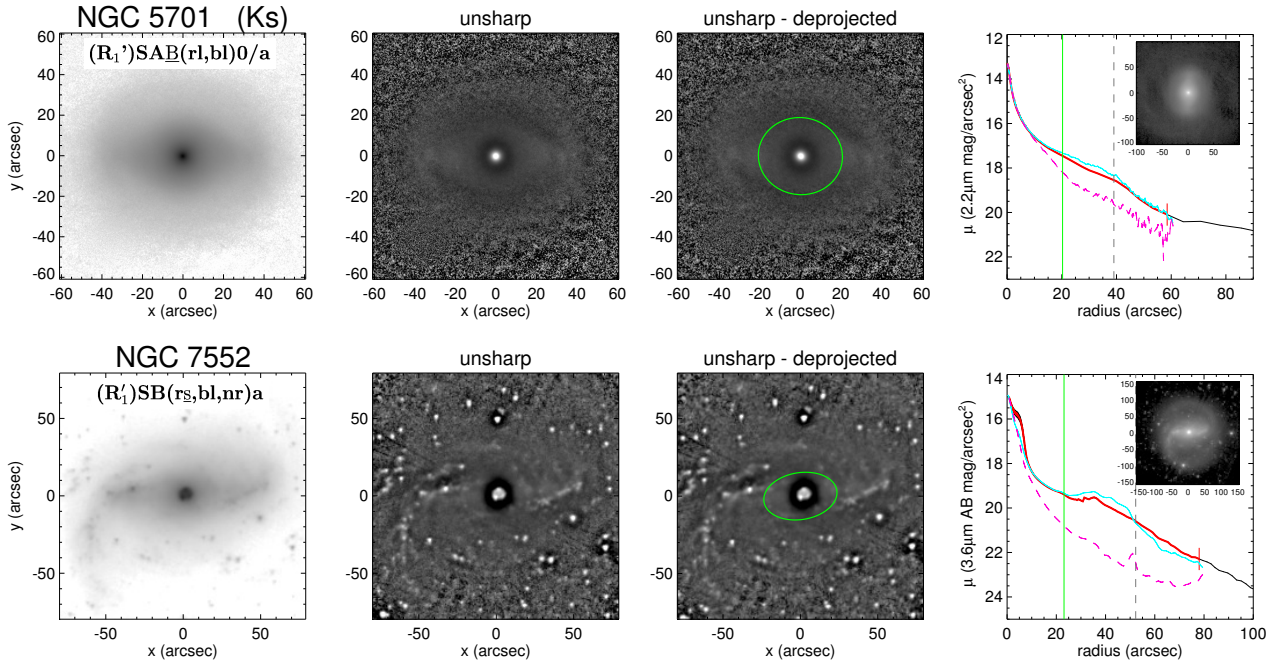


Fig. 21: Two galaxies in our sample, NGC 5701 and NGC 7552, which have detailed stellar population analysis in the literature. The two galaxies are in almost face-on view for which reason the deprojected image is almost the same as the non-deprojected image. The format is the same as in Figure 11.

Table 3: Galaxies without barlenses or X-shape features, mainly unbarred. They are divided to weakly barred (AB), unbarred with inner lenses (A_l), and unbarred without inner lenses (A_{expo}).

Galaxy	Hubble type (Buta et al. 2015)
AB:	
NGC 474	(R')SAB(r'l)0/a pec
NGC 584	SA(l)0$^-$/E(d)2
NGC 1371	(RL)SAB(rs,l)a
NGC 1389	SAB(l,nb)0$^-$
NGC 2681	(RL)SAB(rs)0/a AB
NGC 4267	(L)SAB0$^-$
NGC 4457	(RR)SAB(l)0$^+$
NGC 7098	(R)SAB$_a$(r'l,nb)0/a
IC 2035	SAB(s)0°
A_l:	
NGC 524	(L)SA(l,nl)0°
NGC 1297	SA(rl,l)0°
NGC 1411	(L)SA(l,nl)0°
NGC 2196	SA(l)a
NGC 2300	(R'L)SA(s,l)0°
NGC 2380	SA(l,nl)0$^-$
NGC 3065	(L)SA(l)0°
NGC 3599	SA(l)0°
NGC 3904	SA(l,nl)0$^-$
NGC 3928	SA(l,nl)0$^+$
NGC 4339	SA(r,l)0°
NGC 4459	E2/SA(l)0$^-$
NGC 4489	SA(l)0$^-$
NGC 4503	AB(s,l)°
NGC 4552	SA0-/SA(l)0$^-$
NGC 5273	SA(l,s)0°
NGC 5311	(L)SA(l,nl)0$^-$
NGC 5485	E(dust lane)/SA(l)0$^-$
NGC 5631	E0-1(S4G)/[SA(l)0$^-$]
NGC 5638	SA(l)0-
NGC 5846	E+0/[(L)SA(l,nl)0°]
NGC 5898	(L)SA(l,nl)0$^-$
NGC 6703	(RL)SA(l)0°
NGC 6958	SA(l)0$^-$
NGC 7192	(L)SA(l)0$^-$
NGC 7217	(R')SA(l,nl)0/a
NGC 7377	SA(l)0$^-$
IC 2764	(RL)SA(l)0$^+$
IC 5267	(RL)SA(r,l)0/a
A:	
NGC 3998	SA(r)0°
IC 4329	SA0°/shells/ripples
IC 4991	coreE/[SA0$^-$]

Table 4: The fractions of galaxies with various morphological features in the barlens groups a-g. The classifications of the features are from Buta et al. (2015) and Laurikainen et al. (2011). The second column indicates the fractions of B and AB families, while the number in parenthesis is the total number of galaxies in the group. In other columns the percentage of the galaxies with features is shown together with a binomial uncertainty. By nuclear features we mean nuclear bars and rings. The last column gives the mean galaxy mass in each of the barlens groups. The masses are from Muńoz-Mateos et al. (2015).

bl-grp	B/AB % (N)	r+rl % (N)	l % (N)	R+RL % (N)	L % (N)	nuclear % (N)	ansae % (N)	<logM*/$M_\odot$ >
a	100/... (8)	100±0 (8)	...	37±17 (3)	12±12 (1)	25±15 (2)	12±12 (1)	10.45±0.11
b	75/25 (12)	100±0 (12)	...	92±8 (11)	8±8 (1)	42±14 (5)	17±11 (2)	10.45±0.11
c	85/15 (7)	71±17 (5)	14±13 (1)	42±19 (3)	57±19 (4)	28±17 (2)	57±19 (4)	10.54±0.13
d	100/... (5)	80±17 (4)	...	60±21 (3)	...	100±0 (5)	...	10.86±0.14
e	69/31 (16)	63±12 (10)	12±8 (2)	38±12 (6)	19±10 (3)	50±12 (8)	44±12 (7)	10.66±0.08
f	17/83 (6)	83±15 (5)	...	67±19 (4)	17±15 (1)	50±20 (3)	33±19 (2)	10.75±0.12
g	0/100 (6)	50±20 (3)	17±15 (1)	83±15 (5)	...	33±19 (2)	33±19 (2)	10.45±0.31

Table 5: Similar fractions as given in Table 3, but shown for the parent galaxy groups 1-7.

gal-grp	B/AB % (N)	r+rl % (N)	l % (N)	R+RL % (N)	L % (N)	nuclear % (N)	ansae % (N)	<logM*/$M_\odot$ >
1a	38/62 (8)	50±17 (4)	12±11 (1)	75±15 (6)	25±15 (2)	25±15 (2)	...	10.30±0.19
1b	71/28 (7)	14±13 (1)	14±13 (1)	14±13 (1)	86±13 (6)	14±13 (1)	100±0 (7)	10.48±0.06
2	33/67 (18)	78±10 (14)	17±9 (3)	89±7 (16)	5±5 (1)	56±12 (10)	50±12 (9)	10.58±0.07
3	100/.. (5)	100±0 (5)	...	40±22 (2)	60±22 (3)	20±18 (1)	20±18 (1)	10.83±0.13
4	83/16 (6)	100±0 (6)	...	33±19 (2)	17±15 (1)	50±20 (3)	33±19 (2)	10.22±0.10
5	85/12 (7)	100±0 (7)	...	86±13 (6)	...	86±13 (6)	...	10.71±0.15
6	33/67 (6)	50±20 (3)	16±15 (1)	50±20 (3)	17±15 (1)	50±20 (3)	17±15 (1)	10.70±0.10
7	67/33 (12)	100±0 (12)	...	50±14 (6)	...	33±13 (4)	...	10.55±0.11

Table 6: Cross checking the parent galaxy (1 – 7) and barlens (a – g) groups for the galaxies in which both definitions exist. Notice that both group definitions appear only for a small number of galaxies in our sample.

	1a	1b	2	3	4	5	6	7
a:			1	2	2			2
b:			3	3	2	1		2
c:	1	3	1		1			
d:			1			3	1	
e:	2	2	5	1	2		1	1
f:			2			1	3	
g:	3	1	2					

Table 1: Barlens galaxy sample. Indicated are the galaxy classifications from Buta et al. (2015), and whether the barlens has evidence of boxy isophotes in our isophotal analysis (see Section 3.2): shown are our visual evaluation, and the mean and standard deviation of B_4 within (0.3-1.0) · a_{bl}.

Galaxy	Hubble type (Buta et al. 2015)	visual	$<B_4>$
Strong bars:			
NGC 613	SB(rs,bl,nr)b	no	0.0037±0.0162
NGC 936	(L)SB$_a$(rs,bl)0$^+$	no	0.0054±0.0098
NGC 1015	(R′)SB(r,bl)0/a	no	0.0241±0.0167
NGC 1097	(R′)SB(rs,bl,nr)ab pec	no	0.0180±0.0130
NGC 1300	(R′)SB(s,bl,nrl)b	no	0.0076±0.0161
NGC 1398	(R′R)SB(rs,bl)a	no	0.0014±0.0167
NGC 1433	(R$_1$')SB(r,p,nrl,nb)a	no	-
NGC 1440	(L)SB(rs,bl)0°	no	0.0032±0.0070
NGC 1452	(RL)SB(rs,bl)0/a	no	0.0138±0.0204
NGC 1512	(RL)SB(r,bl,nr)a	no	0.0116±0.0120
NGC 1533	(RL)SB(bl)0°	no	0.0106±0.0085
NGC 1640	(R′)SB$_a$(r,bl)ab	no	0.0032±0.0123
NGC 2787	(L)SB$_a$(r,bl)0°	no	-0.0030±0.0106
NGC 2968	(L)SB(s,bl)0$^+$	no	0.0042±0.0094
NGC 2983	(L)SB$_a$(s,bl)0$^+$	no	-0.0009±0.0043
NGC 3266	(RL)SB(bl)0°	no	0.0117±0.0147
NGC 3351	(R′)SB(r,bl,nr)a	marginal	-0.0005±0.0139
NGC 3384	(L)SAB(bl)0$^-$	marginal	-0.0013±0.0080
NGC 3489	(R)SAB(r,bl)0°:	yes	-0.0099 ±0.0081
NGC 3637	(RL)SB$_a$(rl,bl)0$^+$	no	0.0118 ±0.0155
NGC 3941	(R)SB$_a$(bl)0°	no	0.0073 ±0.0091
NGC 3945	(R)SB$_a$(rl,nl,bl)0$^+$	no	0.0179±0.0448
NGC 3953	SB(r,bl)b	yes	-0.0176±0.0063
NGC 3992	SB(rs,bl,nb)ab	yes	-0.0094±0.0086
NGC 4245	(RL)SB(r,bl,nrl)0$^+$	no	0.0139±0.0115
NGC 4262	(L)SB$_a$(l,bl)0$^-$	no	0.0064±0.0116
NGC 4314	(R$_1$')SB(rl,bl,nr)a	no	0.0173 ±0.0123
NGC 4340	SB$_a$(r,nr,nb,bl)0°	marginal	-0.0124±0.0234
NGC 4371	(L)SB$_a$(r,bl,nr)0$^+$	marginal	-0.0022±0.0191
NGC 4394	(RL)SB(rs,bl,nl)0/a	no	0.0177 ±0.0092
NGC 4448	(R)SB(r,bl)0/a	-	-0.0874±0.0134
NGC 4548	SB(rs,bl)ab	no	0.0070±0.0112
NGC 4579	(RLR')SB(rs,bl)a	no	0.0117 ±0.0126
NGC 4593	(R′)SB(rs,bl,AGN)a	no	0.0105±0.0093
NGC 4596	(L)SB(rs,bl)0/a	no	0.0071±0.0080
NGC 4608	SB(r,bl)0$^+$	no	0.0288±0.0252
NGC 4639	(R′)SAB(rs,bl)ab	no	0.0029 ±0.0067
NGC 4643	(L)SB(rs,bl,nl)0$^+$	no	0.0194±0.0131
NGC 4659	(RL)SAB(l,bl)0°	no	-0.0012±0.0050
NGC 4754	(L)SB$_a$(bl)0°	marginal	-0.0012 ±0.0089
NGC 4795	(R′)SAB$_a$(l,bl)a pec	no	0.0170±0.0227
NGC 5026	(L)SB(rs,nl,bl)a	yes	-0.0189±0.0137
NGC 5101	(R$_1$R$_2$')SB(rs,bl)0/a	no	0.0142±0.0150
NGC 5337	SB(rs,bl)0/a	no	0.0141±0.0144
NGC 5339	SAB(rs,bl)ab	yes	-0.1745±0.0261
NGC 5347	SB(rs,bl)a	no	-0.0037±0.0137
NGC 5375	(R′)SB$_a$(rs,bl)ab	no	0.0103±0.0080
NGC 5701	(R$_1$')SAB(rl,bl)0/a	no	0.0087±0.011
NGC 5728	(R$_1$)SB(r′l,bl,nr,nb)0/a	no	0.0109±0.008
NGC 5850	(R′)SB(r,bl,nr,nb)ab	no	0.0330±0.0190
NGC 5957	(R′)SAB(rs,bl)ab	no	0.0082±0.0150
NGC 6654	(R′)SB$_a$(s,bl)a	no	-
NGC 7079	(L)SAB$_a$(s,bl)0°:	yes	9.27 -0.0074±0.0037
NGC 7552	(R$'_1$)SB(rs,bl,nr)a	no	23.13 -0.0028±0.0185
IC 2051	SB(rs,bl)b	yes	-0.0143±0.0153

Table 1: continued.

Galaxy	Hubble type (Buta et al. 2015)	visual	$<B_4>$
Weak bars:			
NGC 1022	(RL)SAB(rs,bl,ns)0/a	yes	-0.0196±0.0163
NGC 1079	(RL)S(AB$_a$(rs,bl)0°	yes	-0.0064±0.0069
NGC 1201	SAB$_a$(r′l,bl,nb)0°	no	0.0047±0.0060
NGC 1291	(R)SAB(l,bl,nb)0$^+$	no	0.0190±0.0164
NGC 1302	(RLRL)SAB(rl,bl)0$^+$	no	0.0101±0.0113
NGC 1326	(R$_1$)SAB$_a$(r,bl,nr)0$^+$	no	0.0002±0.0080
NGC 1350	(R)SAB$_a$(r,bl)0/a	yes	-0.0099±0.0069
NGC 2273	(R)SAB(rs,bl,nb)a	no	0.0057±0.0225
NGC 2293	SAB$_a$(bl)0/a	no	-0.0065±0.004
NGC 2543	SAB(s,bl)b	yes	-0.0075±0.0145
NGC 2859	(R)SAB$_a$(rl,bl,nl,nb)0$^+$	no	0.0022±0.0077
NGC 3368	(RL)SAB(rs,bl,nl)0°	yes	-0.0038±0.010
NGC 3380	(RL)SAB(rs,bl)0/a	no	0.0018±0.0089
NGC 3892	(RL)SAB(rl,bl)0$^+$	yes	-0.0031±0.0071
NGC 4143	(LR′L)SAB$_a$(s,nb,bl)0°	yes	-0.0027±0.0024
NGC 4454	(RL)SAB(r,bl)0/a	no	0.0082±0.0064
NGC 4503	SAB$_a$(s,bl)0°	marginal	-
NGC 4984	(R′R)SAB$_a$(l,bl,nl)0/a	no	0.0030 ±0.0124
NGC 5134	(R)SAB(rs,bl)a	no	0.0022±0.0108
NGC 5750	(RL)SAB(r′lr,s,bl)0/a	yes	-0.0098±0.0090
NGC 5770	SAB(rl,bl)0$^+$	no	0.0083±0.0132
NGC 5838	(L)SAB(nl,bl)0°	yes	-
NGC 6014	SAB(rs,bl)0/a	no	0.0072±0.0069
NGC 6684	(R′L)SAB(rs,nb,bl)0/a	no	-
NGC 6782	(R)SAB(rl,nr′,nb,bl)0$^+$	no	0.0040±0.0115
Barlens+X:			
NGC5957	(R′)SB(rs,bl)a	no	0.0082±0.0150
NGC3380	(RL)SAB(rs,bl)0/a	no	0.0018±0.0089
NGC3185	(RL)SAB$_{ax}$ (rs,bl)a	yes	-0.0045±0.0036
NGC4902	SB(rs,bl)ab	no	0.0045±0.0103
NGC7421	(R′)SB(rs,bl)ab	no	0.0041±0.0064
IC1067	SB(r,bl)b	no	0.0062±0.0096

Table 2: Sample of galaxies with X-shape features. Shown are the measured semimajor (a_X) and semiminor (b_X) axis dimensions of the X-shape features. The values are mean values of three measurements and their errors are calculated from the standard deviation of the measurents, divided by $\sqrt{3}$. PA_X indicates the position angle of the major axis.

Galaxy	Hubble type (Buta et al. 2015)	a_X (arcsec)	b_X (arcsec)	PA_X (degrees)
ESO 079-003	$SAB_x0/_a$: spw/E(d)5	8.6±0.1	9.1±0.1	311
ESO 404-027	SAB(s)ab:	7.8 ±0.4	5.3±0.1	308
ESO 443-042	S_x0/a spw/E(d)8	15.7±0.0	12.0±0.1	308
IC 0335	$S0^-$[c] sp/E(d)7	5.1±0.1	4.3±0.1	263
IC 1067	SB(r,bl)b	7.6±0.1	5.5±0.1	327
IC 1711	SAB_x0^+: sp	5.9±0.2	9.3±0.1	222
IC 3806	$SA(r)0^+$	3.2±0.0	3.3±0.1	0
IC 4237	SB(r)b	3.3±0.1	2.7±0.0	299
IC 5240	$SB_x(r)0/a$	12.3±0.3	5.7±0.2	272
NGC 532	$SAB_{xa}(r)0/a$	12.3±0.1	8.3±0.2	208
NGC 615	$(R')SA_x(r)ab$	8.9±0.2	5.9±0.1	339
NGC 660	$SAB_{xa}ab$/PRG	14.4±0.4	10.9±0.4	225
NGC 779	$(L)SA_x(rs)a$	8.5±0.2	5.5±0.1	342
NGC 955	SAB_x0^+	7.9±0.2	6.9±0.2	198
NGC 1461	SAB(r)0°	27.4±0.9	17.3±0.2	337
NGC 1476	Im sp	5.7±0.3	4.1±0.2	266
NGC 2549	$SB_x0°$ sp	4.9±0.1	2.9±0.1	359
NGC 2654	SB_x(r,nd)0/a sp	16.5±0.1	12.1±0.2	244
NGC 2683	$(R'L)SB_{xa}(rs)0/a$ sp	26.2±0.4	20.6±0.2	222
NGC 3098	$S0^-$ sp/E8	5.2±0.0	4.4±0.1	269
NGC 3185	$(RL)SAB_{ax}$(rs,bl)a	12.6±0.2	8.6±0.1	300
NGC 3190	SAB_x(l,nd)0/a sp pec	11.3±0.51	10.4±0.2	294
NGC 3227	SAB_x(s)a	20.9±0.4	9.9±0.2	331
NGC 3254	$SAB_{xa}b$	9.4±0.1	6.6±0.2	230
NGC 3301	$(R'L)SAB_x(r)0^+$ sp	15.0±0.5	7.1±0.1	235
NGC 3380	(RL)SAB(rs,bl)0/a	6.3±0.2	5.5 ±0.1	200
NGC 3424	S_xab: sp pec	10.6±0.3	7.3±0.2	291
NGC 3623	$(R')SAB_x(rs)a$	29.6±0.8	15.9±0.5	352
NGC 3628	SB_x(nd)bc sp/E(b)8 pec	53.0±2.0	33.3±0.6	284
NGC 3673	$(R')SAB_x(rs)ab$	16.7±0.1	11.6±0.2	257
NGC 3692	(R'L)SA(r)0/a sp	6.8±0.1	4.5±0.0	274
NGC 3887	$(RL)SAB_x(rs)bc$	9.4±0.4	9.0±0.3	359
NGC 4013	SAB_xa spw/E(d)7	16.1±0.3	13.6±0.1	246
NGC 4123	$SB_x(rs)ab$	10.6±0.2	6.2±0.2	285
NGC 4192	$(R_1')SAB_x$(rs,nd)ab	37.1±0.9	28.6±0.7	332
NGC 4216	$(R_2')SAB_{ax}$(r,nd)ab sp/E7-8	34.0±0.6	23.4±0.56	200
NGC 4220	$(L)SAB(r)0^+$	10.0±0.1	8.2±0.1	316
NGC 4235	S_x0^+ sp	14.9±0.7	12.9±0.1	229
NGC 4268	$SAB(rs)0^+$: sp	11.6±0.4	8.7±0.8	228
NGC 4293	$R(L)SB_x(rs)0/a$	18.8±0.9	14.4±0.5	256
NGC 4302	SB_{xa}?[0/a]bc sp/E7	14.4±0.3	11.0±0.1	359
NGC 4343	$(R')SAB(r)0/a$ sp/E2	6.7 ±0.1	3.4±0.1	314
NGC 4419	SAB_x0/a sp/E6	6.8±0.2	6.9±0.4	312
NGC 4429	$SAB_x(r,nl)0^+$	23.9±0.5	18.3±0.4	276
NGC 4435	S0° sp/SB0° sp	7.1±0.1	5.2±0.1	189
NGC 4462	$SAB_x(rs)a$	11.1±0.2	8.5±0.0	304
NGC 4488	$SB_x(s)a$	20.1±0.7	9.7±0.9	327
NGC 4565	$SB_x(r)ab$ spw	25.2±0.3	30.0±0.7	314
NGC 4569	$(R'L)SAB_x(rs,x_1r)a$	24.8±0.4	16.3 ±0.6	196
NGC 4586	$SAB_x(s,nd)0/a$ sp	19.8 ±0.4	19.6±0.8	293
NGC 4710	$SB_{xa}(nd)0^+$ sp/E(d)7	21.5±0.4	17.4 ±0.3	207
NGC 4725	$(R')SAB_x(r,nb)a$	43.9±0.6	33.4 ±0.9	217
NGC 4818	$(RL)SAB_{xa}(s)0°$	10.3±0.3	9.0±0.2	190
NGC 4845	$(R'L)SAB_x(r'l,nd)0/a$	22.9±0.1	19.4±0.9	257
NGC 4856	$(RL)SB0^-$	11.4±0.4	6.8±0.2	220
NGC 4902	SB(rs,bl)ab	8.3±0.1	6.4±0.2	245

Table 2: continued.

Galaxy	Hubble type (Buta et al. 2015)	a_X (arcsec)	b_X (arcsec)	PA_X (degrees)
NGC 5005	$(R_2')SAB_{xa}(rs)ab$	13.0±0.2	9.7±0.1	251
NGC 5022	$S_{ax}\underline{ab}$: sp	6.0±0.1	5.0±0.2	203
NGC 5073	$SA\underline{B}_{xa}0/a$ sp	14.3±0.1	11.1±0.3	330
NGC 5145	$(R:)SA(r,nl)0^+$	3.5±0.0	4.3±0.1	264
NGC 5170	$(R')SAB_x(r\underline{l})0/a$ sp	13.3±0.8	9.9 ±0.3	306
NGC 5297	$SAB_x(s)bc$ sp	6.8±0.1	6.1±0.1	333
NGC 5353	$SB_{xa}0^+$ sp	9.6±0.1	4.4±0.2	324
NGC 5377	$(R_1')SAB_{xa}(r'l,nl)0/\underline{a}$	23.4±0.9	17.4±0.3	219
NGC 5422	$SA\underline{B}_{ax}0^+$ sp	14.7±0.4	8.8±0.1	333
NGC 5443	$(R'L)SAB_x(rs)a$ sp	11.6±0.5	8.4±0.3	215
NGC 5448	$(R_1L)SAB_x(\underline{r}s)a$	14.5±0.9	10.7±0.5	287
NGC 5529	SB_xab spw	13.2±0.1	11.8±0.2	295
NGC 5689	$(R'L)SAB_x(r'l,nd)\underline{0}/a$	8.0±0.3	8.5±0.2	267
NGC 5746	$(R')SB_x(r,nd)0/a$ sp	22.5±0.4	22.7±0.6	351
NGC 5757	$(R')SB(rs)\underline{a}b$	5.0±0.3	5.6±0.1	341
NGC 5777	$(R)S_x(l,nd)\underline{0}/a$ sp	5.9±0.1	5.6±0.1	322
NGC 5806	(R'L)SAB(rs,nrl)ab	15.4±0.3	11.4±0.3	358
NGC 5854	$(RL)SA\underline{B}_x(rl)0^+$ sp	6.9±0.2	5.8±0.3	238
NGC 5864	$(R\underline{L})SB_{xa}0^+$ sp	9.8±0.2	7.7±0.1	239
NGC 5878	$SAB_{xa}(rs)ab$	11.0±0.3	7.5±0.4	180
NGC 5916	SAB(s)a pec	6.2 ±0.2	6.0±0.0	207
NGC 5957	$(R')SB(\underline{r}s,bl)a$	8.4±0.2	6.9±0.2	270
NGC 7140	$(R')SA\underline{B}_x(rs,nrl)a\underline{b}$	19.0±0.5	12.1±0.2	195
NGC 7163	$SAB_x(s)a$	13.2±0.5	8.5±0.3	274
NGC 7171	$SAB_x(s)b$	6.9±0.3	5.2±0.1	293
NGC 7179	$SB_{xa}(\underline{r}'l)0/a$	9.6±0.2	6.1±0.3	224
NGC 7183	$SA\underline{B}_{xa}0/a$ sp pec/E(d)7	20.0±0.4	13.9±0.1	259
NGC 7332	SB_x0^o	12.12±0.2	10.2±0.3	339
NGC 7421	$(R')SB(rs,bl)ab$	6.0±0.1	5.67 ±0.2	270
NGC 7513	(R'L)SB(rs)a	8.8±0.3	6.3±0.1	251
NGC 7531	$SAB_x(r)a$	12.3±0.2	7.1±0.1	194
PGC 45650	$SA\underline{B}_a(s)ab$	4.3±0.1	5.6±0.2	268

/